Evaluating Stochastic Parameter Perturbations in Convection-Permitting Ensemble Forecasts of Lake-Effect Snow

W. MASSEY BARTOLINI[a] AND JUSTIN R. MINDER[a]

[a] *University at Albany, State University of New York, Albany, New York*

(Manuscript received 29 July 2024, in final form 10 January 2025, accepted 5 March 2025)

ABSTRACT: Lake-effect snowstorms can produce large snowfall accumulations that are challenging to simulate and forecast. One source of forecast uncertainty for these events is the uncertain parameterization of subgrid processes, such as planetary boundary layer and surface layer (PBL/SL) turbulence and cloud and precipitation microphysics (MP), in numerical weather prediction models. One way to quantify this uncertainty is to design ensembles that use stochastic parameter perturbations (SPPs) to vary individual uncertain parameters within physics schemes. This research aims to evaluate and improve the utility of SPP for convection-permitting ensemble forecasts of lake-effect snow, with a focus on PBL/SL and MP parameterizations. We focus on a snowfall event observed during the Ontario Winter Lake-effect Systems (OWLeS) field campaign, which is simulated with 1-km horizontal grid spacing using the Weather Research and Forecasting Model. A suite of 20-member ensemble simulations are run, including ensembles where SPP is applied only to PBL/SL or MP, where SPP is applied to multiple schemes concurrently, where perturbations to initial and boundary conditions (ICs/BCs) are applied instead of SPP, and where SPP and IC/BC perturbations are applied together. SPPs produce substantial spread in simulated precipitation, despite having only modest impacts on the synoptic-scale flow. They accomplish this by modulating lake–atmosphere fluxes, boundary layer characteristics, precipitation growth processes, and hydrometeor terminal fall speeds. The spread and skill of simulated precipitation from an ensemble using SPP alone is comparable to that from ensemble that uses IC/BC perturbations alone. The physical pathways whereby SPPs generate spread are examined and discussed.

KEYWORDS: Snowfall; Cloud microphysics; Probabilistic Quantitative Precipitation Forecasting (PQPF); Mesoscale models; Stochastic models; Lake effects

1. Introduction

In many regions, lake-effect snowstorms (LeSs) are an important part of cold season weather. Such storms often produce heavy snowfall in localized regions immediately downwind of the Laurentian Great Lakes of North America and other major lakes around the world (e.g., Niziol et al. 1995; Nakai et al. 2005; Laird et al. 2009; Alcott et al. 2012; Norris et al. 2013; Steenburgh and Nakai 2020). Societal impacts from these LeS events can be severe, with disruptions to commerce and transportation and even loss of life. For example, a cold air outbreak across much of the contiguous United States in late December 2022 was accompanied by intense lake-effect snows in the Buffalo, New York, area, with 2-day snowfall totals in excess of 100 cm and wind gusts of over 30 m s^{-1} resulting in blizzard conditions, stranded motorists, and over 40 deaths (Smith 2023).

To better understand and predict such events, the Ontario Winter Lake-effect Systems (OWLeS) field campaign was conducted during the winter of 2013–14 (Kristovich et al. 2017). Focused on the area downwind of Lake Ontario, including the Tug Hill Plateau (hereafter Tug Hill), OWLeS studied lake-effect precipitation and microphysical processes as well as land–atmosphere interaction and boundary layer convection downwind of the Great Lakes. The campaign featured numerous in situ and remote sensing observations, including ground-based and airborne scanning and profiling radars, rawinsondes, airborne cloud physics instruments, and manual precipitation measurements, which collected data during 24 intensive observing periods (IOPs). Research from OWLeS has revealed insights into convective organization of LeS, including the roles of convective-to-stratiform transition over land (Minder et al. 2015; Welsh et al. 2016), Tug Hill orography (Campbell et al. 2016; Veals et al. 2018; Gowan et al. 2022), solenoidal secondary circulations (Bergmaier et al. 2017; Bergmaier and Geerts 2020), and land–breeze fronts (Campbell and Steenburgh 2017; Steenburgh and Campbell 2017; Gowan et al. 2021). These studies highlight the need for convection-permitting simulations, using fine horizontal grid spacing [O(1) km, if not smaller] to resolve many of the important processes that shape lake-effect storms.

To improve prediction of LeS, studies have focused on different aspects of numerical weather prediction (NWP), including the uncertainties associated with model physics and initial and boundary conditions (ICs/BCs). For example, total precipitation amounts can vary by as much as a factor of 2 depending on either the microphysics (MP) scheme (Reeves and Dawson 2013; Bartolini 2019; Gaudet et al. 2021) or the planetary boundary layer and surface layer (PBL/SL) schemes used (Conrick et al. 2015; Fujisaki-Manome et al. 2017; Bartolini 2019; Minder et al. 2020). Other model uncertainties include sensitivity to horizontal grid spacing between convection-permitting [O(1) km] and large-eddy simulations [O(100) m], which affect band morphology, updraft strength, and the degree of hydrometeor riming (Jensen et al. 2020).

Corresponding author: Justin R. Minder, jminder@albany.edu

DOI: 10.1175/WAF-D-24-0141.1

Additionally, the representation of lake ice cover and lake surface temperature in model ICs/BCs can strongly influence the placement and intensity of LeS bands (Zhao et al. 2012; Wright et al. 2013; Xue et al. 2017).

One way of accounting for uncertainties in LeS prediction is to design convection-permitting ensemble forecasts that perturb model physics and/or ICs/BCs to generate an ensemble of plausible forecasts that can serve as a basis for probabilistic forecasts. Here, we focus on representing model physics uncertainty using stochastic parameter perturbations (SPPs; e.g., Berner et al. 2015; Jankov et al. 2017, 2019). This approach perturbs individual parameters within one or more physics schemes. Perturbations are scaled using a stochastically generated pattern that varies in space and time, with individual parameter perturbations constrained using observational and/or physical limits. Kalina et al. (2021) describe the configuration of the High-Resolution Rapid Refresh Ensemble (HRRRE), which uses both SPP and IC/BC perturbations. Results from this and other experimental ensembles are being used to inform the design and future operational implementation of a single-physics ensemble replacing the current convection-permitting multiphysics ensemble [High-Resolution Ensemble Forecast (HREF); Roberts et al. 2020]. HRRRE has been evaluated primarily during warm season experiments across the central United States, with SPP increasing near-surface ensemble spread in thermodynamic variables and improving precipitation forecast reliability (Kalina et al. 2021).

Some aspects of ensemble design for lake-effect forecasts have been investigated. For example, Saslo and Greybush (2017) ran both IC/BC and multiphysics ensemble simulations of OWLeS IOP2b. They found that GEFS ICs/BCs produced greater ensemble dispersion than regional ensemble Kalman filter ICs with impacts on band position and intensity. Their results showed that including members with different physics schemes in their ensemble configuration primarily affected LeS precipitation intensity rather than band position. Gaudet et al. (2021) investigated the predictability of a different OWLeS case, IOP4, running an MP ensemble using both different MP schemes and parameter perturbations to a single habit-aware MP scheme. Their MP ensemble results showed that precipitation variations were mostly related to differences in precipitation-type partitioning between snow and graupel.

This study builds on previous research by evaluating the utility of SPP as a technique for generating convection-permitting ensemble forecasts of lake-effect snow, a specific application of SPP that has yet to be investigated. We explore this topic using ensemble simulations of an OWLeS case study. Our baseline model configuration is loosely based on the experimental HRRRE, to which we add additional SPP within the microphysics scheme that targets uncertainty in snow properties. The baseline configuration is compared to different ensemble configurations to explore combinations of stochastic physics and IC/BC perturbations. Ensemble simulations are evaluated against observations from OWLeS, to assess their accuracy, and compared against each other, to better understand how different model uncertainties limit the predictability of LeS and generate ensemble spread. Section 2 describes the model configuration and observational datasets used as well as the verification methodology. Section 3 discusses ensemble results from case-study simulations. Section 4 concludes by summarizing results and discussing implications for ensemble forecast system design.

2. Data and methods

In this study, we investigate the predictability of lake-effect precipitation in a LeS case impacting the Great Lakes region during the OWLeS field campaign from 10 to 12 December 2013 (IOP2b). This case was chosen because it was well observed by OWLeS assets, produced large snowfall totals, and has been extensively studied in previous literature (e.g., Campbell et al. 2016; Saslo and Greybush 2017; Campbell and Steenburgh 2017; Steenburgh and Campbell 2017; Bergmaier et al. 2017; Bartolini 2019; Minder et al. 2020; Jensen et al. 2020). The results presented here are based on the work originally presented in the PhD thesis Bartolini (2023), which also includes a similar analysis of a second OWLeS case.

a. *Ensemble configuration*

All simulations in this study use the Weather Research and Forecasting (WRFv4.2.2) Model, version 4.2.2 (Skamarock et al. 2008). A triply nested set of limited area domains is centered on Lake Ontario, with the inner domain including all of Lake Ontario and key downwind topographic features such as Tug Hill and the western Adirondack Mountains (Fig. 1a). These domains use horizontal grid spacings of $\Delta x = 12$, 4, and 1.33 km. Two-way nesting is used between the parent and nested domains. The intermediate and outer domains encompass the remainder of the Great Lakes to represent upstream LeS bands which can affect conditions over Lake Ontario (e.g., Laird et al. 2017; Kristovich et al. 2018; Lang et al. 2018). However, the coarser grid spacing on the intermediate, 4 km, domain may limit the realism of such simulated lake-to-lake influences. Fifty-one vertical levels are used in all simulations, with vertical grid spacing ranging from 20 m near the ground to 520 m aloft. On the outer domain, convection is parameterized using the Grell–Freitas scheme (Grell and Freitas 2014), while the inner two domains are convection permitting. The model physics configuration emulates that of the HRRR (version 4; Dowell et al. 2022), including use of the Thompson–Eidhammer (TE) MP (Thompson and Eidhammer 2014) and Mellor–Yamada–Nakanishi–Niino (MYNN) level 2.5 PBL/SL schemes (Nakanishi and Niino 2006).

All ensembles use ICs/BCs from the Global Ensemble Forecast System (GEFS), with a 6-h BC update interval (NOAA-National Center for Environmental Prediction 2017). However, bottom BCs over the Great Lakes, specifically lake–surface temperature and ice cover, are supplied from nowcasts generated by the NOAA Great Lakes Coastal Forecasting System (GLCFS; Chu et al. 2011; NOAA Great Lakes Environmental Research Laboratory 2014), following methodology used in previous studies (Campbell et al. 2016; Bartolini 2019; Minder et al. 2020).

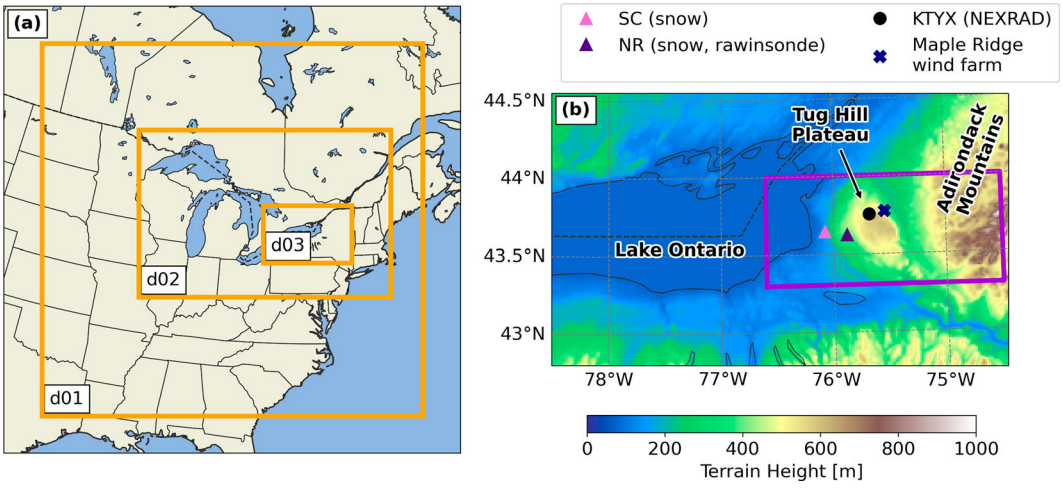

FIG. 1. (a) WRF Model domains used for simulations, (b) geography of eastern Lake Ontario and the Tug Hill Plateau region, with terrain height (shaded) and operational and research instrument locations during OWLeS (markers), including the SC and NR field sites and the local NEXRAD operational radar (KTYX). The purple box in (b) shows the domain used for ensemble statistics in Figs. 5, 6, and 14.

A suite of 20-member ensemble simulations are run to examine the contributions of SPP and IC/BC perturbations to the forecast evolution (Table 1). All experiments are initialized from GEFS forecasts at 1200 UTC 10 December 2013, allowing for 12 h of model integration prior to the primary lake-effect period of interest, and run for 42 h. As a reference for comparison, a single additional deterministic forecast (CTRL) is also run using unperturbed ICs/BCs from GEFS ensemble member 0 and no SPP. The GEFS_ICBC ensemble only includes perturbed ICs and BCs, allowing for the comparison of the impacts of IC/BC perturbations with those from SPP, various combinations of which are included in the other ensembles.

A variety of ensembles are run using SPP. All of these experiments use perturbations from a stochastic 2D pattern generator, which generates patterns with specified spatial and temporal correlation (as in Jankov et al. 2017). We use a perturbation pattern decorrelation length scale of 150 km and a perturbation pattern decorrelation time scale of 72 h, consistent with the most recent configuration of HRRRE (I. Jankov, NOAA GSL, 2021, personal communication). The ALLSPP and ALLSPP_ICBC ensembles mimic HRRRE by including SPPs to a range of schemes, including the TE14 MP scheme (following Thompson et al. 2021) and the MYNN PBL/SL schemes (following Jankov et al. 2017). However, motivated by the results of Bartolini (2023), additional MP perturbations in TE14 are applied that target snow processes, specifically snow mass–diameter, fall speed–diameter, and capacitance parameterizations (see the appendix for details). To isolate the sensitivity to specific perturbed processes, ensembles are run where SPP is only applied to MP (SPP_MP), only applied to turbulence parameterizations (SPP_TURB), or only applied to subcomponents of these (SPP_SL_HDF, SPP_MP_SNMV, described in section 3e).

b. *Observations*

Manual snowfall measurements from OWLeS are used to assess the accuracy of radar-based quantitative precipitation estimates and to evaluate model forecasts in the region of heaviest snowfall. Snowfall observations were collected at

TABLE 1. Summary of the ensemble configurations used. All ensembles with SPP use a decorrelation length scale of 150 km and a decorrelation time scale of 72. The specific SPPs applied in each ensemble are noted, using abbreviations: microphysics (MP), only snow mass and fall velocity (SNMV) relations, horizontal diffusion (HDF), planetary boundary layer (PBL) turbulence, surface layer (SL) turbulence, land surface model (LSM), and convection (CONV; only active on outer domains).

Abbreviation	ICs and BCs	SPP.	Notes
SPP_TURB	GEFS ens00	SPP–TURB	Includes PBL, SL, HDF, and gravity wave drag perturbations
SPP_SL_HDF	GEFS ens00	SPP–TURB	Includes SL, HDF, and gravity wave drag perturbations only
SPP_MP	GEFS ens00	SPP–MP	Includes existing and new perturbations
SPP_MP_SNMV	GEFS ens00	SPP–MP	Includes only perturbations to snow *M–D* and *V–D* coefficients
ALLSPP	GEFS ens00	SPP–TURB, MP, LSM, CONV	Includes existing and new perturbations
GEFS_ICBC	GEFS ens01-20	None	
ALLSPP_ICBC	GEFS ens01-20	SPP–TURB, MP, LSM, CONV	Includes existing and new perturbations

Sandy Creek (SC) and North Redfield (NR) sites on the western part of Tug Hill during OWLeS (Fig. 1b). At these sites, manual observations of snow depth and liquid precipitation equivalent (LPE) were collected at 6-h intervals (Steenburgh et al. 2014a,b). Additional LPE observations around the Tug Hill region were sourced from the Global Historical Climatology Network–Daily (GHCN-D) dataset (Menne et al. 2012a,b). GHCN-D precipitation observations are only collected every 24 h, so some lake-effect precipitation that fell during the start of the first day of GHCN-D observations (1200 UTC 10 December 2013–1200 UTC 11 December 2013), before the start of IOP2b, is included in the GHCN-D total LPE for each site. However, this excess precipitation is generally less than 10%–15% of the event total for IOP2b, so it is left in the GHCN observation amounts during verification.

Gridded quantitative precipitation estimates (QPEs) are computed using data from the NEXRAD WSR-88D radar at Montague, New York (KTYX). KTYX level II base reflectivity data for each case were downloaded from the NEXRAD archive hosted by Amazon Web Services (NWS 1991). From this, QPE is calculated using the relationship of Vasiloff (2001): $Z = 75S^2$, where Z is the reflectivity ($mm^6\ m^{-3}$) and S is the liquid equivalent snowfall rate ($mm\ h^{-1}$), applied to the base reflectivity data for each case study. This approach follows the methodology used by Campbell et al. (2016) and Bartolini (2019) for the same case, with the specific Z–S relationship selected because it best matched OWLeS manual observations, albeit with some underestimation at SC (Campbell et al. 2016).

Upper-air soundings launched at North Redfield, New York (NR; Fig. 1b), during OWLeS (Steenburgh et al. 2014c) are used to evaluate WRF-simulated thermodynamic and wind profiles within LeS bands.

c. *Verification methodology*

Ensemble precipitation forecasts are verified against the two OWLeS manual observation sites (SC and NR) and the available GHCN-D observations, using a nearest-neighbor approach to select the model grid point closest to each station. Root-mean-square error (RMSE) and mean absolute error (MAE) are computed using ensemble mean values for all sites.

3. Results

a. *Event overview*

OWLeS IOP2b took place on 10–12 December 2013, during a period of upper-level westerly flow and broad synoptic-scale troughing across the Great Lakes (Figs. 2a,b). Two shortwave troughs were embedded in the large-scale flow, aiding large-scale ascent during this period. Following the passage of the first shortwave trough on 10 December, westerly flow developed across the Great Lakes with weak cold air advection on 11 December (Figs. 2c,d). Lake surface conditions were largely ice free during this event, with only partial ice cover in bays such as Green Bay, Saginaw Bay, and northwestern Georgian Bay (Minder et al. 2020, their Fig. 1b). Lake surface temperatures ranged from 5° to 9°C, with the warmest conditions found in the southern Lake Michigan and central Lake Ontario (Minder et al. 2020). Combined with 850-hPa temperatures from around −15° to −18°C, lake surface to 850-hPa temperature differences were around 24°C. This is substantially more than the 13°C minimum threshold used by forecasters to assess the potential for lake-effect convection (Niziol et al. 1995).

A steady period of LeS developed downwind of Lake Ontario early on 11 December and persisted for about 24 h until approximately 0030 UTC 12 December. Examples of LeS band structures observed by the KTYX radar are shown in Fig. 3. As discussed in Campbell et al. (2016), LeS exhibited both weakly banded and nonbanded broad coverage morphologies (e.g., Figs. 3a,b), with two transient periods of more-organized long-lake-axis-parallel banding (e.g., Fig. 3c). After 0300 UTC 12 December, boundary layer winds became more northwesterly over Lake Ontario behind the second shortwave trough passage (Fig. 2d), causing the primary band downwind of Lake Ontario to shift southward (Fig. 3c) and dissipate along the southern shoreline of Lake Ontario by 0700 UTC 12 December (not shown).

Radar-based QPE from KTYX shows the axis of heaviest precipitation extending from Lake Ontario across central Tug Hill into the western Adirondacks, showing good agreement with manual and gauge measurements over the western slopes of Tug Hill (Fig. 4). Due to the persistence of the LeS bands under westerly flow, the heaviest 24-h precipitation amounts were quite localized, in excess of 60 mm over the center of Tug Hill including 64 mm observed at North Redfield. KTYX radar beam interference with the Maple Ridge wind farm on the northeast portion of Tug Hill causes spuriously high QPE amounts in excess of 70 mm, much larger than nearby gauge observations. QPE amounts farther from the radar, over the eastern slopes of Tug Hill and western Adirondacks and over Lake Ontario, are more uncertain due to few direct observations and potential radar beam overshooting of the shallow LeS bands (e.g., Brown et al. 2007).

b. *Comparison of ensemble precipitation*

Ensemble precipitation forecasts for OWLeS IOP2b are summarized in Figs. 5 and 6 for ensemble mean and spread, respectively. In the mean, all ensembles have excellent placement of the axis of heaviest precipitation over Tug Hill with relatively minor biases in precipitation amounts compared to KTYX QPE for this event (Figs. 4 and 5). However, each ensemble mean underforecasts windward precipitation over Tug Hill and overforecasts precipitation leeward of Tug Hill into the western Adirondacks (although leeward QPE is uncertain).

Ensemble spread is greatest along the axis of maximum precipitation, peaking over Tug Hill (Figs. 6a–e). Large differences in spread can be seen between the various ensemble configurations. The largest spread is found in the ensemble that combines SPP with IC/BC perturbations (ALLSPP_ICBC). When used in isolation, the full suite of SPPs (ALLSPP) produces about 20% more spread than IC/BC perturbations

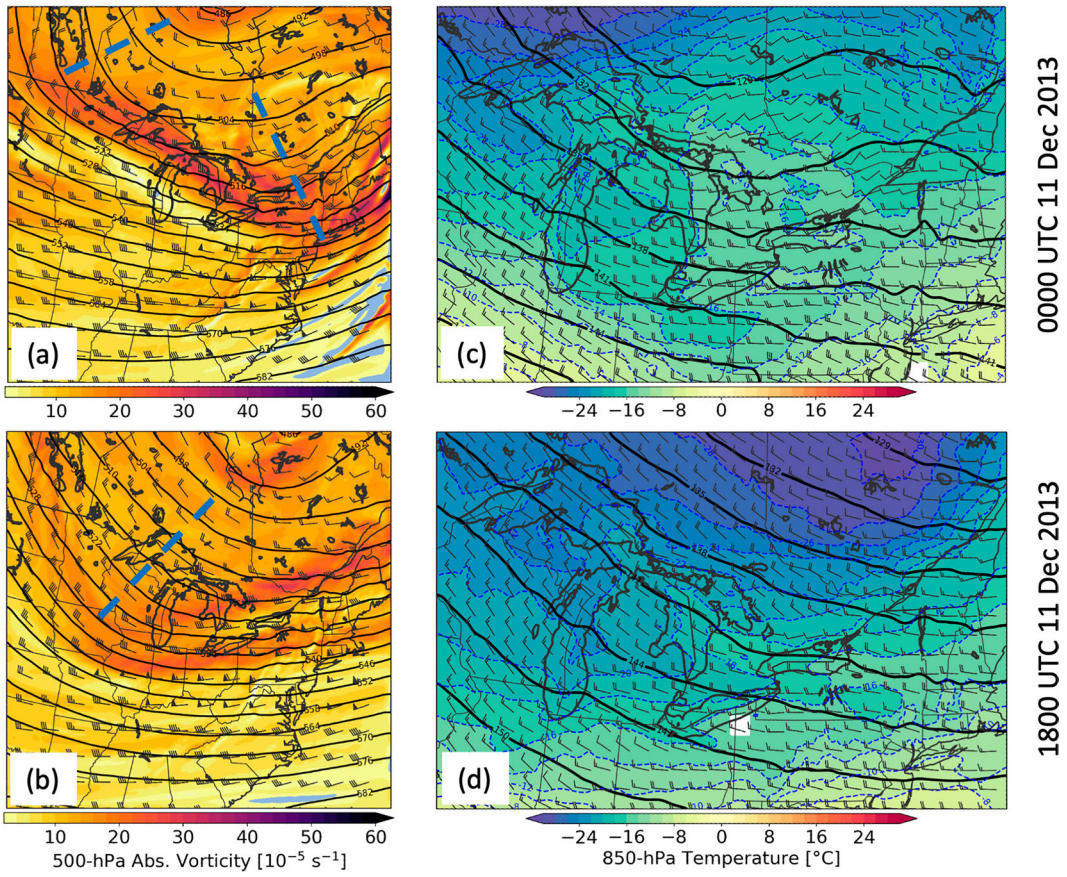

FIG. 2. Synoptic evolution of OWLeS IOP2b: (a),(b) 500-hPa wind (barbs; m s^{-1}), geopotential height (contours; dam), absolute vorticity (fill), and trough axes (dashed blue lines); (c),(d) 850-hPa wind (barbs; m s^{-1}), geopotential height (black contours; dam), and temperature (fill/dashed contours; °C). All panels are taken from the CTRL forecast.

(GEFS_ICBC), illustrating the sensitivity of LeS to physics uncertainty. When further isolating SPPs to individual schemes, perturbations to turbulent mixing (SPP_TURB) are found to contribute greater spread than perturbations to microphysics (SPP_MP). The spread contributions from various perturbations do not combine linearly, in that the sum of spread from isolated perturbations is greater than the spread resulting from applying the perturbations concurrently.

For each ensemble, the verification of 24-h ensemble mean precipitation at observation sites is plotted in Fig. 7. Values from the closest model grid point to each observation location are used to calculate these statistics. RMSE and MAE have only small variations between ensembles, consistent with the similar ensemble mean precipitation patterns in Fig. 5. The similar error statistics across ensembles shows that ensemble mean precipitation forecasts are not degraded by the inclusion of SPP.

Ensemble spread [quantified by the ensemble standard deviation (STDEV)] and spread/skill ratio (STDEV/RMSE) are also plotted in Fig. 7. In contrast to RMSE and MAE, spread has large variations across ensembles, consistent with the differences in spread shown in Fig. 6. The spread/skill ratio is used as a simple metric for evaluating ensemble spread relative to model error. In a "perfect ensemble," a ratio near 1 is expected (e.g., Buizza 1997), such that ensemble spread is predictive of model error. Larger values suggest an overdispersive ensemble, and lower values suggest an underdispersive ensemble. Figure 6 suggests that all ensembles considered here are underdispersive (spread/skill ratio < 1). The ensembles with best spread/skill ratio (closest to 1) are those with the highest spread, namely, ALLSPP_ICBC and ALLSPP, since RMSE is nearly constant across all ensembles. This highlights the positive contribution of SPP to the overall ensemble performance, consistent with other ensemble configuration studies conducted for different weather types (e.g., Romine et al. 2014; Jankov et al. 2017, 2019).

c. *The role of band position*

We hypothesize that north–south band position variability is one of the primary drivers of event-total precipitation differences between individual ensemble members. To test this, band positions are analyzed for all members of each ensemble and for the KTYX QPE estimates, at each forecast

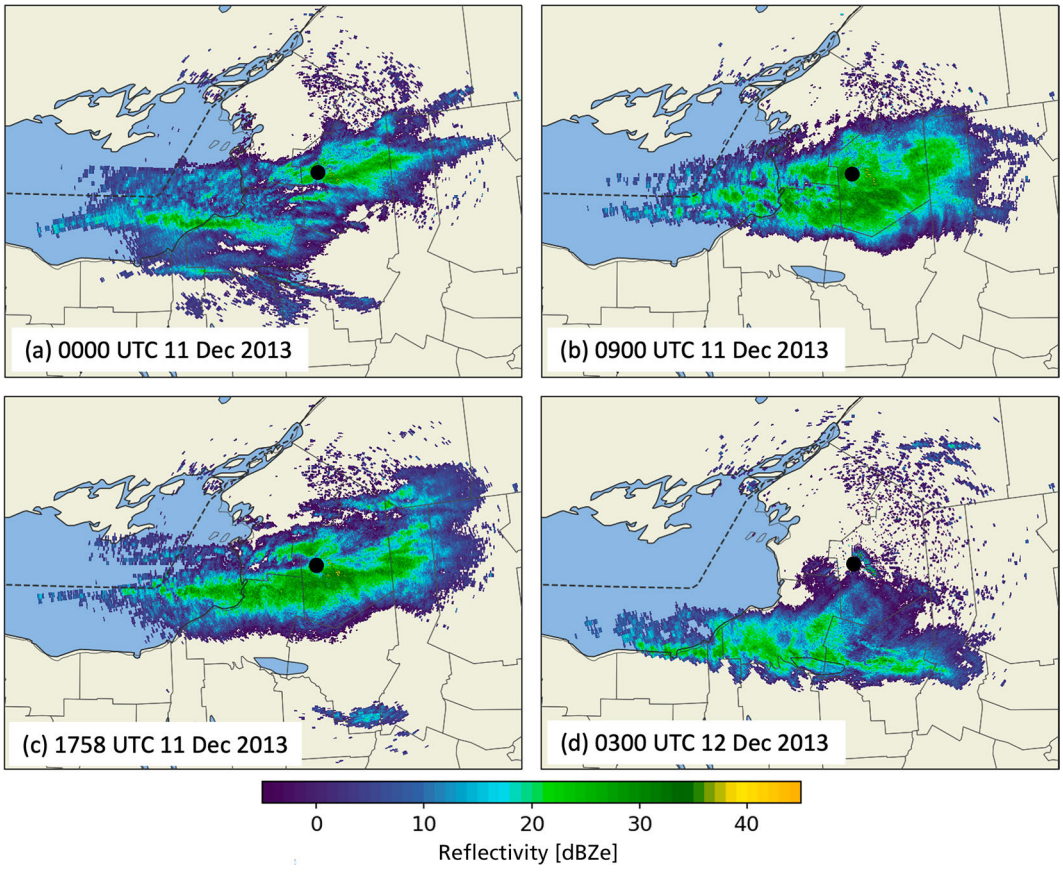

FIG. 3. KTYX NEXRAD base reflectivity (0.5° elevation) observations during OWLeS IOP2b. The location of the KTYX radar is shown with a black circle. Thin black lines show county boundaries.

hour by calculating the precipitation mass centroid latitude y_p from 1-h accumulated precipitation, where

$$y_p = \frac{\sum_{i=1}^{N_x}\sum_{j=1}^{N_y} p_{i,j} y_{i,j}}{\sum_{i=1}^{N_x}\sum_{j=1}^{N_y} p_{i,j}}. \quad (1)$$

In this calculation, $p_{i,j}$ and $y_{i,j}$ are the hourly precipitation and latitude at a single grid point (i, j), respectively. The terms N_x and N_y are the number of grid points in the x and y directions for the green bounding box in Fig. 8. This box is chosen to focus on LeS bands over and downstream of Lake Ontario.

Figure 8 shows time series of precipitation mass centroid latitude for each ensemble, compared with the centroids derived from radar QPE. To connect band position differences to variations in overlake boundary layer flow, area-average 925-hPa wind direction is calculated within a box encompassing most of eastern Lake Ontario (purple box in Fig. 8) for each forecast hour of each ensemble member and compared with 3-hourly analyses from the RAP model (Benjamin et al. 2016). Overall, band positions remain quasistationary over Tug Hill for most of the event (through 1800 UTC 11 December), with only small variations in band position across all of the ensembles. Despite some discrepancies in the timing of north–south band shifts during the period from 2100 UTC 10 December through 0600 UTC 11 December, all ensemble members are generally within 15 km of KTYX-observed band latitudes. Simulated wind direction at 925 hPa is westerly throughout most of the event, consistent with the mostly stationary band position and single long-lake-axis-parallel band structure associated with maximized long-axis fetch across Lake Ontario. After 2100 UTC 11 December, band positions shift southward across the ensembles as 925-hPa flow turns northwesterly, associated with the arrival of a shortwave trough crossing the Great Lakes (Figs. 2b,d). The southward shift is accompanied by reduced precipitation rates as overlake fetch distances are reduced under northwest flow. Compared to KTYX observations, the simulated bands shift southward too early, with observed band latitude falling outside of the solution envelope for all ensemble configurations after approximately 0000 UTC 12 December 2013. This southward bias in band position appears to be caused by a bias in the simulated wind direction, with most ensemble members showing winds that are increasingly more northerly than the RAP-analyzed winds during this time period, which may relate to errors in the simulated phase speed of the approaching shortwave trough.

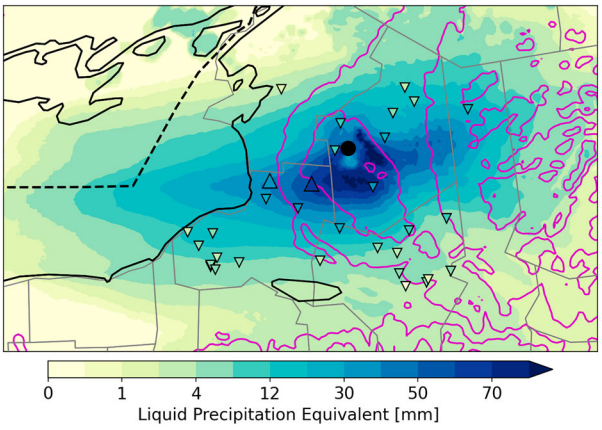

FIG. 4. KTYX-based QPE (mm) during OWLeS IOP2b, for the 24-h period ending at 0000 UTC 12 Dec 2013. A black circle indicates the location of KTYX. Manual snow survey and GHCN observations around the Tug Hill region are denoted by upward- and downward-pointing triangles, respectively, and are color coded by total precipitation according to the same color scale as QPE. Magenta contours represent the model terrain height every 200 m. Thin gray lines show county boundaries.

Spread in north–south band position and wind direction varies between ensembles. Ensemble spread in band position and winds are comparable between the ALLSPP and the GEFS_ICBC ensemble, indicating that the suite of SPPs have a similarly large impact on LeS band position as IC/BC perturbations, via their impact on wind direction. Ensemble spread in band position and wind direction is larger for the SPP_TURB ensemble than for SPP_MP, suggesting that PBL perturbations are the dominant source of band position uncertainty in the ALLSPP configuration, driven by larger variations in the lower-tropospheric wind direction. While some additional spread in band latitude is gained in combining stochastic and IC/BC perturbations (ALLSPP_ICBC), the overall amount of spread in band position and wind direction is less than the sum of the individual component ensembles. Overall, ensembles with large band position spread correspond to those with large total precipitation spread (Fig. 6), supporting the hypothesis that north–south band position differences explain much of the variability in precipitation between ensemble members.

The temporal evolution of spread varies across ensemble configurations. Ensembles with IC/BC perturbations have moderate spread as early as 1200 UTC 10 December which gradually increases with time. SPP-only ensembles (e.g., SPP_TURB and ALLSPP) have less spread than GEFS_ICBC through approximately 0600 UTC 11 December but increase in spread with forecast hours until they approach the amount of spread in GEFS_ICBC by the end of the event. These results suggest that SPP takes longer to affect band position than IC/BC perturbations.

The relationship between LeS band position and overlake wind direction is quantified by a correlation analysis between simulated 1-h band centroid latitude and lake-average 925-hPa wind direction (Fig. 9). All ensembles exhibit a strong correlation ($r^2 > 0.75$) between band position and wind direction, with southward shifts in band position toward the end of IOP2b strongly associated with winds backing from westerly to

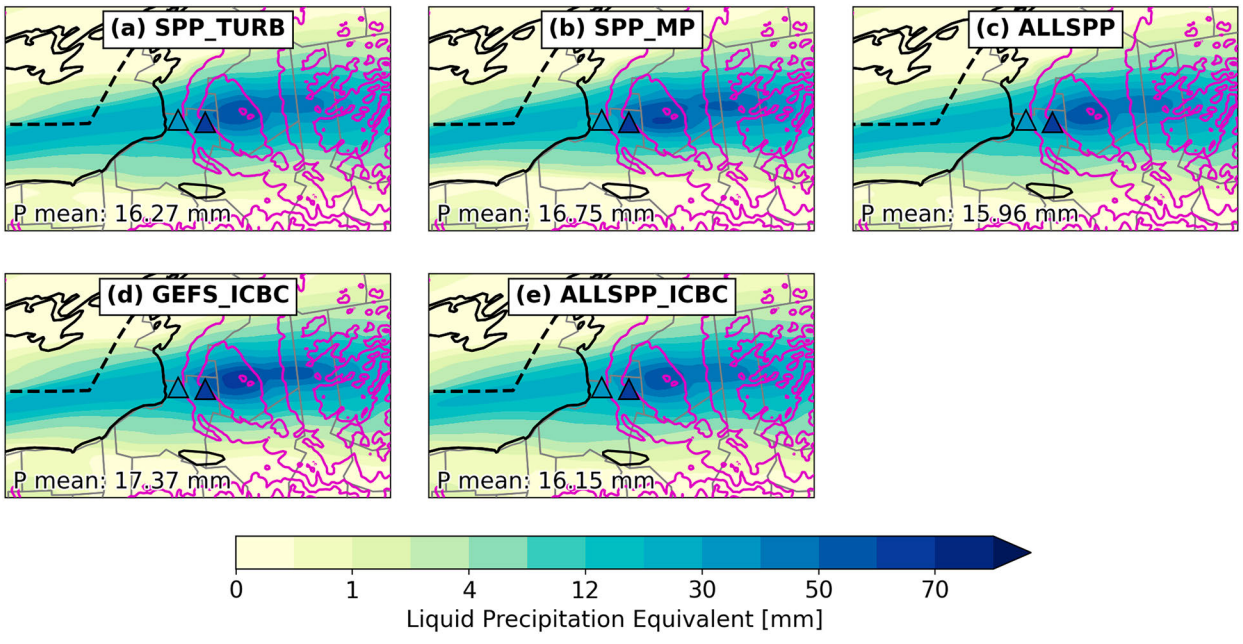

FIG. 5. Ensemble mean precipitation (fill) for the 24-h period ending at 0000 UTC 12 Dec 2013: (a)–(e) forecast precipitation for select ensembles from Table 1. Observed LPE amounts from two manual observing sites are plotted on all panels following the same color scale (triangles). Mean precipitation values are given for each ensemble, averaging over the box shown in Fig. 1b. Magenta contours represent the model terrain height, every 200 m.

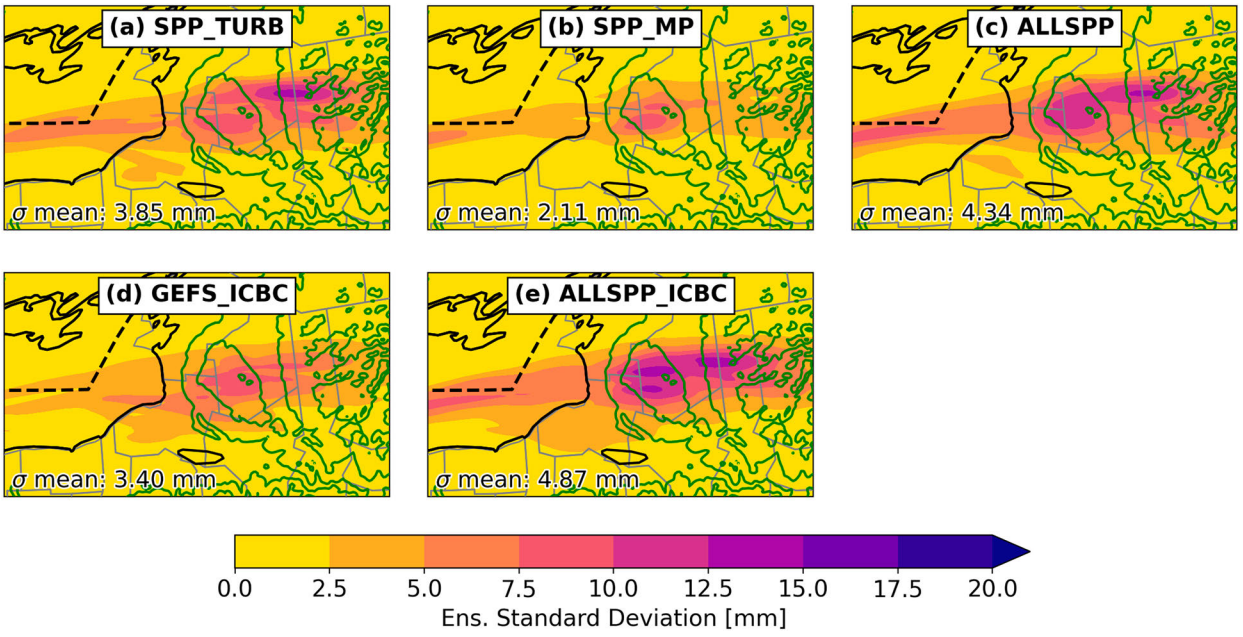

FIG. 6. As in Fig. 5, but for ensemble STDEV of precipitation (fill) for the 24-h period ending at 0000 UTC 12 Dec 2013. Area-average precipitation STDEV values are plotted for each ensemble, averaging over the box shown in Fig. 1b. Green contours represent the model terrain height, every 200 m.

northwesterly after 0000 UTC 12 December. The highest correlation values are found in SPP ensembles (e.g., SPP_TURB, SPP_MP), which have the lowest overall forecast spread.

d. *Evaluating differences in spread between IC/BC and physics perturbations*

To better understand the character and causes of variations in precipitation spread between ensembles, we compare forecasts from individual members in the GEFS_ICBC and ALLSPP ensembles. Figure 10 shows GEFS_ICBC ensemble member 24-h precipitation differences relative to CTRL (Fig. 10b), to highlight variations in precipitation between members. While several modes of variability are evident among the members, the most distinct one is a north–south dipole of increased/decreased precipitation relative to CTRL (e.g., members 6, 15, 19, and 20), which corresponds to north–south band position uncertainty among the ensemble members as analyzed in Fig. 8.

Figure 11 shows ALLSPP ensemble member 24-h precipitation differences. While some ALLSPP members exhibit a north–south dipole in precipitation (e.g., members 4, 5, 18),

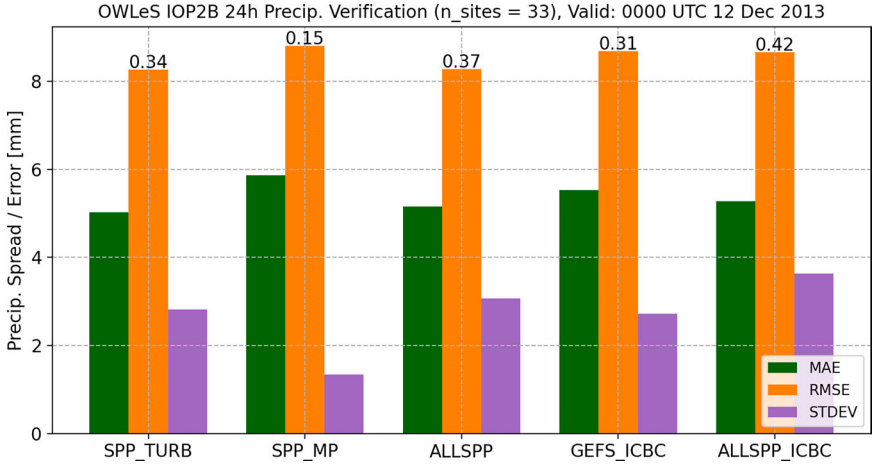

FIG. 7. Ensemble 24-h precipitation verification for the period ending at 0000 UTC 12 Dec 2013. MAE and RMSE are computed for each ensemble mean across all OWLeS snow survey and GHCN gauge locations. Ensemble STDEV is calculated as the average STDEV across all observation locations. Spread/skill (STDEV/RMSE) ratios for each ensemble are labeled.

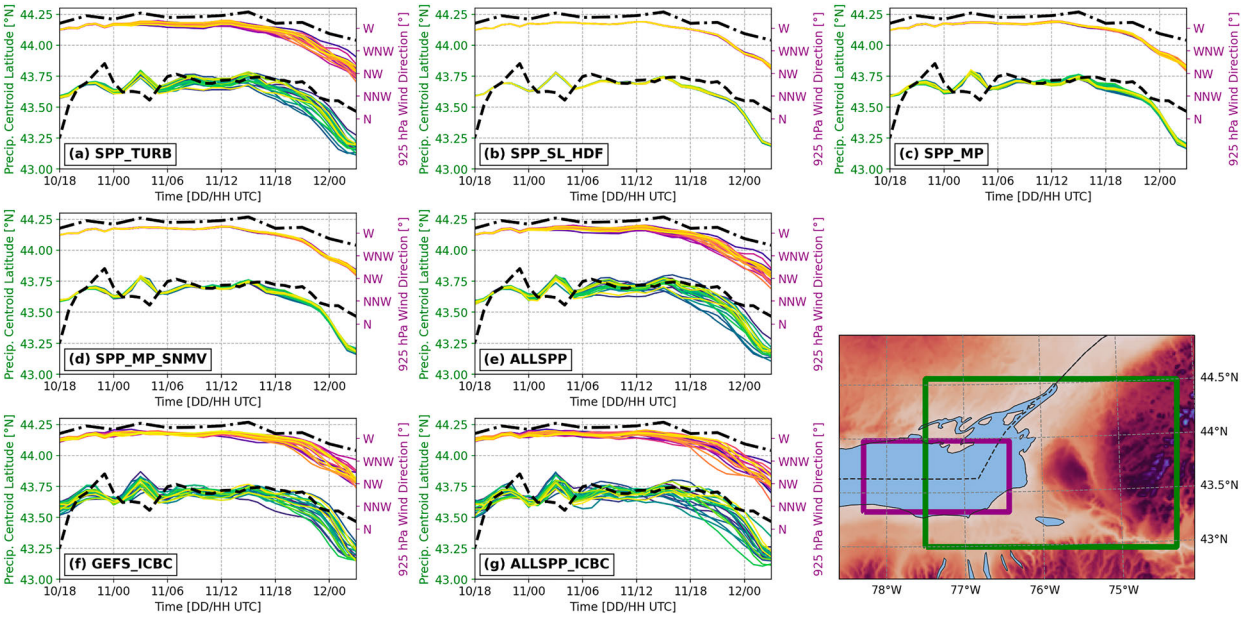

FIG. 8. (a)–(g) Time series of 1-h precipitation mass centroid latitude and lake-average 925-hPa wind direction for each ensemble forecast. Individual members are plotted with different colored lines, with lighter colors indicating higher number ensemble members. Black dashed lines represent observed precipitation centroid latitude from KTYX radar observations. Black dash–dotted lines show the 925-hPa winds from RAP analyses (3-h interval). Inset map shows the areas used for averaging wind direction (smaller purple box) and calculating precipitation centroids (larger green box). Panels (b) and (d) are discussed further in section 3e.

many members have overall magnitude differences not resembling a dipole (e.g., members 2, 7, 17) with the largest differences skewed toward less precipitation (e.g., member 7). While these differences can be partially explained by band position variability among members (Fig. 8e), ALLSPPs appear to produce additional impacts on precipitation intensity. Precipitation spread is largest over and downwind of Tug Hill, suggesting that the inland extent of heavy precipitation is particularly sensitive to physics perturbations.

To better understand how differences in precipitation spread relate to synoptic conditions, we compare synoptic-scale spread between GEFS_ICBC and ALLSPP ensembles. For these ensembles, Fig. 12 shows ensemble spread for several fields relevant to LeS: 500-hPa geopotential height, 850-hPa temperature, and 12-h average surface sensible heat flux. The valid time shown, 1200 UTC 11 December 2013 (forecast hour 24), is near peak observed LeS band intensity and is representative of ensemble spread at other nearby forecast hours.

Aloft, 500-hPa height spread is largest over and downwind of the Great Lakes, in a region extending from Michigan to New England, highlighting flow uncertainty just ahead of a shortwave trough axis (Figs. 12a,b). However, spread is about an order of magnitude larger in GEFS_ICBC than ALLSPP, suggesting that the contribution of SPP to forecast spread in the 500-hPa flow is minimal relative to GEFS_ICBC perturbations for forecast lead times less than 48 h.

Closer to the surface, when considering 850-hPa temperature, spread differences between ALLSPP and GEFS_ICBC are more comparable (Figs. 12c,d). ALLSPP has roughly 50%–75% of the 850-hPa temperature spread found in GEFS_ICBC. While GEFS_ICBC has several spread maxima across the entire forecast domain, ALLSPP spread is largest near the Great Lakes, likely representing uncertainty in the timing and magnitude of cold air advection over the lakes.

At the surface, where simulated lake-average upward sensible heat fluxes average 300–400 W m^{-2}, spread values of 20–40 W m^{-2} represent substantial variations to surface forcing for LeS (Figs. 12e,f). Averaging across all overwater grid points, surface flux spread is nearly identical between ALLSPP and GEFS_ICBC, though differences in spread across individual lakes can be seen. Surface moisture flux spread comparisons between the ensembles are similar to those for sensible heat flux (not shown). The surface flux spread in these two ensembles is generated by two distinct physical pathways. GEFS_ICBC produces substantial spread in synoptic-scale flow across the Great Lakes, with associated variations in low-level cold air advection over the lakes leading to spread in surface fluxes. The effects of ALLSPP are more localized, as they are primarily generated by directly perturbing parameterized surface and boundary layer mixing.

To investigate differences in environmental profiles between the two ensembles, forecast soundings, valid at 1700 UTC 11 December 2013, are compared to an observed sounding at North Redfield (Fig. 13). The observed sounding is located within the LeS band core (Fig. 2f), while ensemble member soundings are either within or near the simulated LeS band core, depending on the simulated band position. The observed sounding had erroneous humidity measurements, so only observed temperature is plotted.

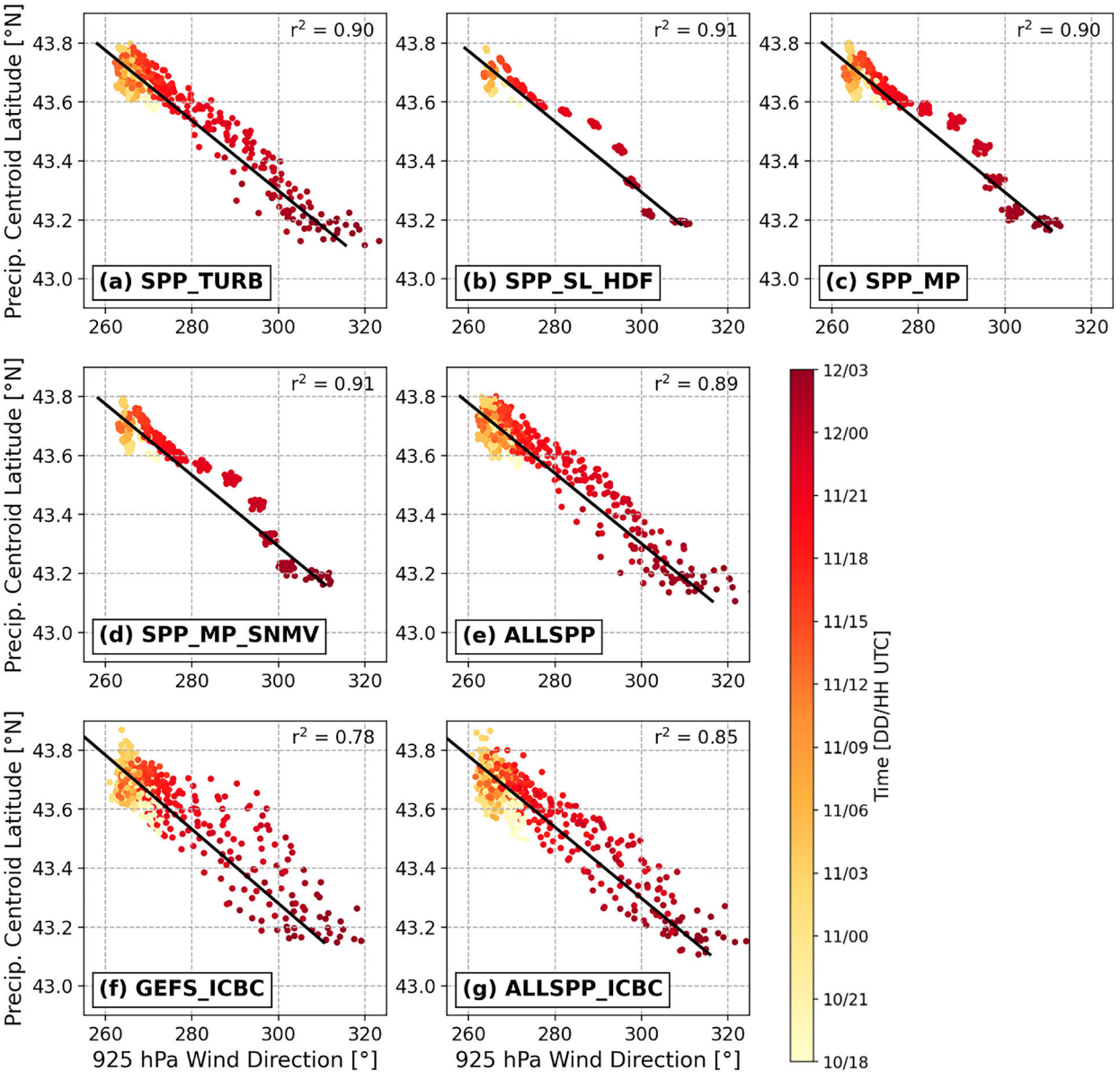

FIG. 9. Correlation analysis of 1-h precipitation mass centroid latitude vs lake-average 925-hPa wind direction for each ensemble forecast during OWLeS IOP2b. Markers are color coded by forecast hour. Black lines depict least squares linear regressions for each ensemble across the entire forecast period, with the coefficient of determination values plotted on each panel.

Both ensembles generally capture the observed thermodynamic structure and wind profile within the LeS band core, with a primary capping inversion around 680 hPa and westerly winds throughout the troposphere. Small errors can be seen when comparing simulated capping inversion heights to observations, with ALLSPP inversion heights biased low. However, the observed inversion height is within the forecast spread of both ensembles. Similarly, while forecast wind profiles vary slightly among the ensemble members, the observations are within the ensemble spread. While spread in ALLSPP is comparable to that of GEFS_ICBC within the PBL (below 700 hPa), GEFS_ICBC spread is much larger than SPP spread through the mid- and upper troposphere. This is consistent with the synoptic-scale spread differences between the ensembles in Fig. 12. These sounding results indicate the large sensitivity of PBL thermodynamics in LeS events to both stochastic physics and IC/BC perturbations.

Overall, the results of section 3d further illustrate how spread in ALLSPP is primarily driven by microscale and mesoscale "bottom-up" physics perturbations. These perturbations are most active near the surface, where parameterized PBL/SL/MP processes are active. In contrast, spread in GEFS_ICBC is driven by "top–down" perturbations. These affect synoptic-scale flow aloft, which in turn affects PBL

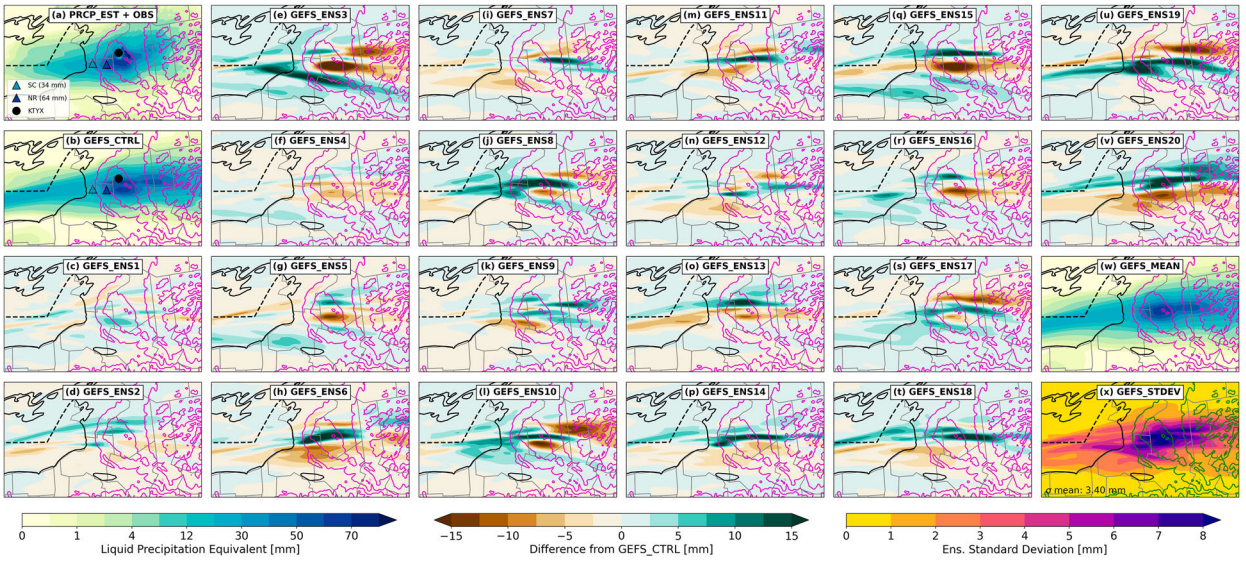

FIG. 10. The 24-h total precipitation forecasts from each of the 20 members in GEFS_ICBC plus the CTRL simulation. (a) KTYX-based QPE (fill) with snow survey observations (markers) using the same color scale, (b) CTRL forecast total precipitation, (c)–(v) precipitation forecast differences (fill) for each member relative to CTRL, calculated as ensemble member minus CTRL, (w) 20-member ensemble mean precipitation (fill), and (x) ensemble STDEV of precipitation (fill). Solid contours denote the model terrain height, every 200 m.

processes near the surface through resulting variations in low-level thermodynamics and winds.

e. *SPP sensitivity experiments*

In this section, the role of SPP applied to PBL/SL and MP is analyzed in more detail by investigating two additional ensembles, SPP_SL_HDF and SPP_MP_SNMV, with a reduced set of perturbations to PBL/SL and MP parameters (see Table 1). The goal of these experiments is to better understand the behavior of SPP–PBL and SPP–MP in LeS forecasts by isolating the specific parameters and parts of the stochastic perturbation suites that produce the most ensemble spread.

1) ROLE OF SURFACE LAYER VERSUS PLANETARY BOUNDARY LAYER TURBULENCE

We hypothesize that perturbations to the SL parameterization are the primary source of spread in precipitation and surface fluxes, with perturbations to PBL fluxes playing a secondary role. We base this on the previously documented strong sensitivity of LeS to surface fluxes in the high flux and steep low-level

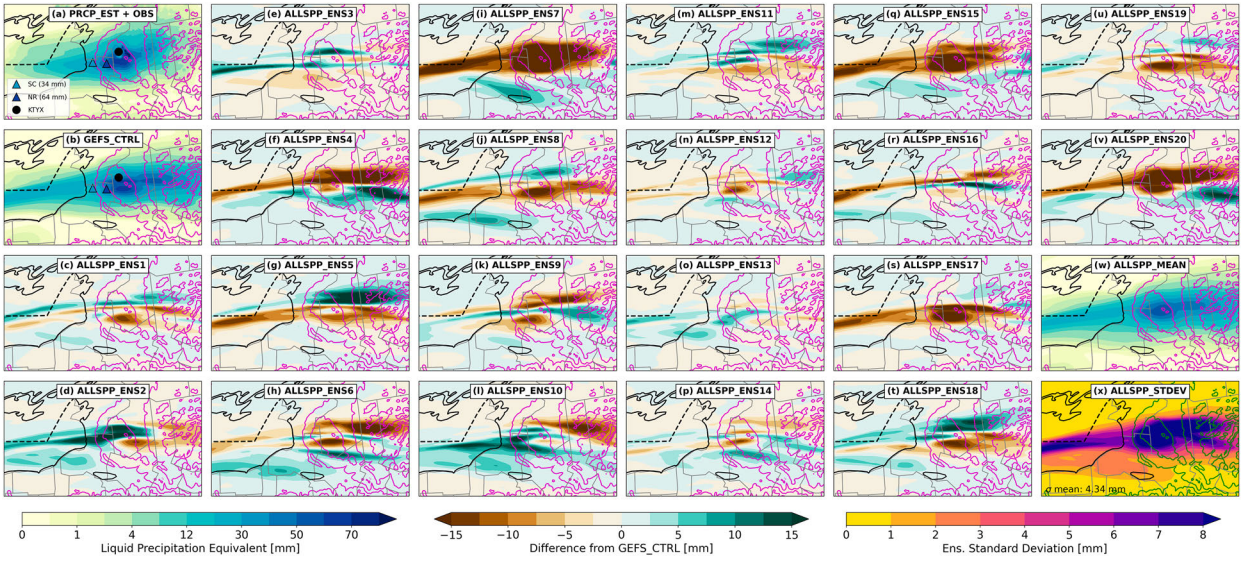

FIG. 11. As in Fig. 10, but for the ALLSPP ensemble.

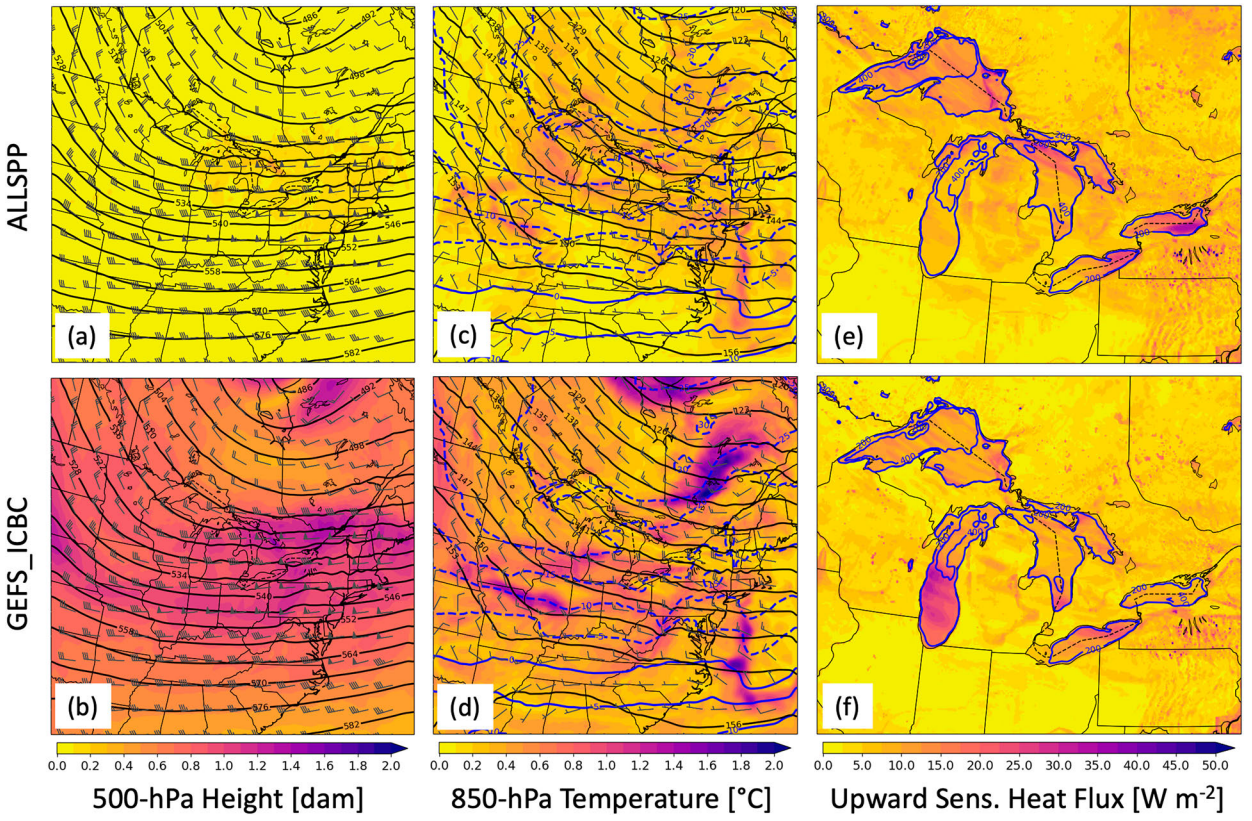

FIG. 12. Ensemble spread comparison of several forecast fields from domain 2. All plotted fields are valid at 1200 UTC 11 Dec 2013. (a),(b) Ensemble mean 500-hPa geopotential height (contours; dam), ensemble STDEV of 500-hPa geopotential height (fill; dam), and ensemble mean 500-hPa wind (barbs; m s^{-1}). (c),(d) Ensemble mean 850-hPa temperature (blue contours; °C), ensemble STDEV of 850-hPa temperature (fill; °C), ensemble mean 850-hPa geopotential height (black contours; dam), and ensemble mean 850-hPa wind (barbs; m s^{-1}). (e),(f) Ensemble mean 12-h average upward sensible heat flux (contours; W m^{-2}) and ensemble STDEV of 12-h average upward sensible heat flux (fill; W m^{-2}).

lapse rate environment over the Great Lakes (e.g., Gerbush et al. 2008; Conrick et al. 2015; Bartolini 2019; Minder et al. 2020). To test this hypothesis, we analyze results from the SPP SL HDF ensemble, a modified version of SPP_TURB, where PBL perturbations are disabled [leaving only SL, horizontal diffusion (HDF), and gravity wave drag perturbations active], and compare results from this ensemble to the previously presented SSP_TURB ensemble. HDF and gravity wave drag perturbations are not expected to contribute strongly to forecast spread in either ensemble, leading us to leave these active in both ensembles.

Figures 14a–f show ensemble forecast 24-h precipitation mean and standard deviation results for the pair of SPP–PBL sensitivity experiments. Overall, both SPP_TURB and SPP_SL_HDF have accurate placement of the heaviest precipitation axis across Tug Hill, with SPP_SL_HDF having slightly increased maximum precipitation amounts in excess of 60 mm (Fig. 14b). However, large differences in ensemble spread are found between the ensembles, with SPP_SL_HDF having nearly an order of magnitude smaller spread than SPP_TURB. This indicates a relatively larger role of PBL flux perturbations as compared to SL perturbations in generating spread, refuting our above hypothesis. To better understand why SPP_SL_HDF has so little spread, variations in LeS band position, PBL thermodynamics, and surface fluxes are analyzed.

Differences in ensemble member forecast band position and wind direction between SPP_TURB and SPP_SL_HDF are described in Fig. 8. Consistent with the greatly reduced total precipitation spread in SPP_SL_HDF relative to SPP_TURB, spread in precipitation centroid latitude and wind direction is nearly zero for SPP_SL_HDF (Fig. 8b). Both ensembles have a high correlation ($r^2 < 0.9$) between north–south band position and 925-hPa wind direction (Figs. 9a,b). Together, the high correlation and clustering of ensemble members indicate that SPP_SL_HDF has almost no variation in mesoscale/synoptic-scale flow among its ensemble members, suggesting that this lack of variability in flow direction and, in turn, band position is a primary factor contributing to low spread in total precipitation. Reduced spread is not limited to precipitation or wind direction variables in SPP_SL_HDF, as temperature spread is reduced throughout the depth of the PBL (Bartolini 2023). Sensible heat flux spread over the Great Lakes is around 30–50 W m^{-2}

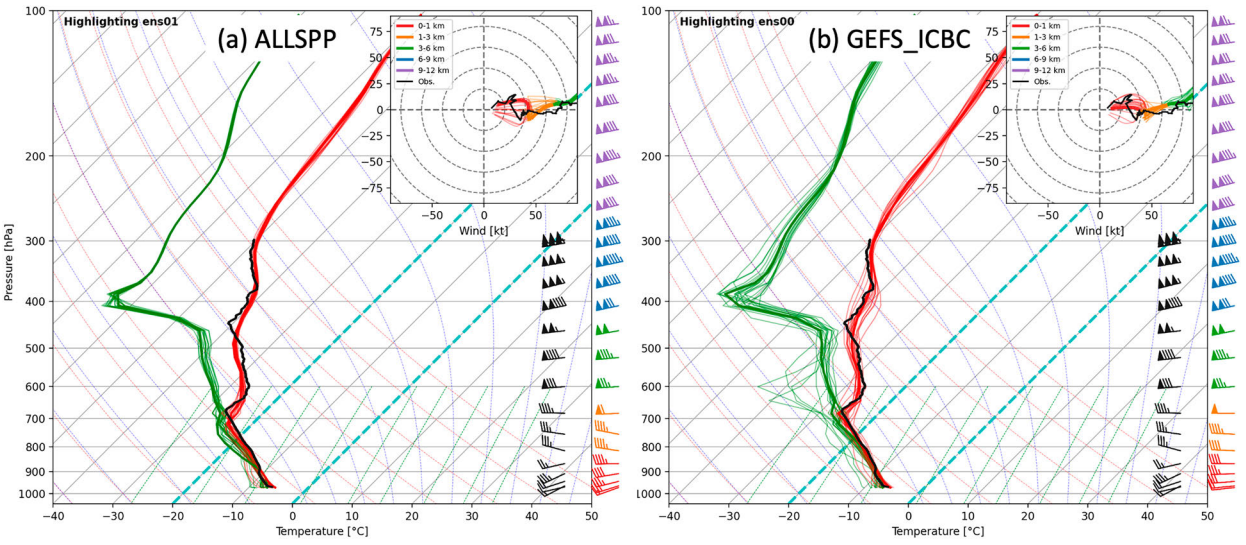

FIG. 13. Skew T–log$p$ diagram comparison of ensemble forecast soundings to an observed sounding at NR at 1727 UTC 11 Dec 2013 during OWLeS IOP2b. Ensemble forecasts are taken from the nearest model grid point to NR at 1700 UTC, with individual members plotted using red and green lines for temperature and dewpoint, respectively. Observed temperatures are denoted by black lines, with the observed wind profile denoted by black barbs and black line in the hodograph inset. A single member from each ensemble is highlighted with thicker temperature and dewpoint lines, with wind barb profiles from that member shown in colors.

in SPP_TURB, while it is only 2–5 W m^{-2} in SPP_SL_HDF (not shown).

To attribute the low spread in SPP_SL_HDF to specific processes, we analyze the individual variables perturbed in the MYNN SL scheme as well as their perturbation magnitudes. Within the SPP–SL scheme, momentum z_0, thermal $z_{0,t}$, and moisture roughness lengths $z_{0,q}$ have stochastic perturbations applied. Specifically, z_0 is perturbed by ±20% for one standard deviation, while $z_{0,t}$ and $z_{0,q}$ are perturbed by ±10% for one standard deviation (Kalina et al. 2021, their Table 1). In turn, these perturbations modulate surface sensible heat and moisture fluxes through the following equations, shown here for sensible heat flux F_H:

$$F_H = C_h \rho_a c_p u(\theta_o - \theta), \tag{2}$$

$$C_h = \frac{u_* \kappa}{P_R u\left[\ln\left(\frac{z + z_{o,h}}{z_{o,h}}\right) - \psi_h\right]}, \tag{3}$$

where ρ_a is the air density; u is the horizontal wind speed; and θ is the potential temperature, from the lowest model grid cell z.

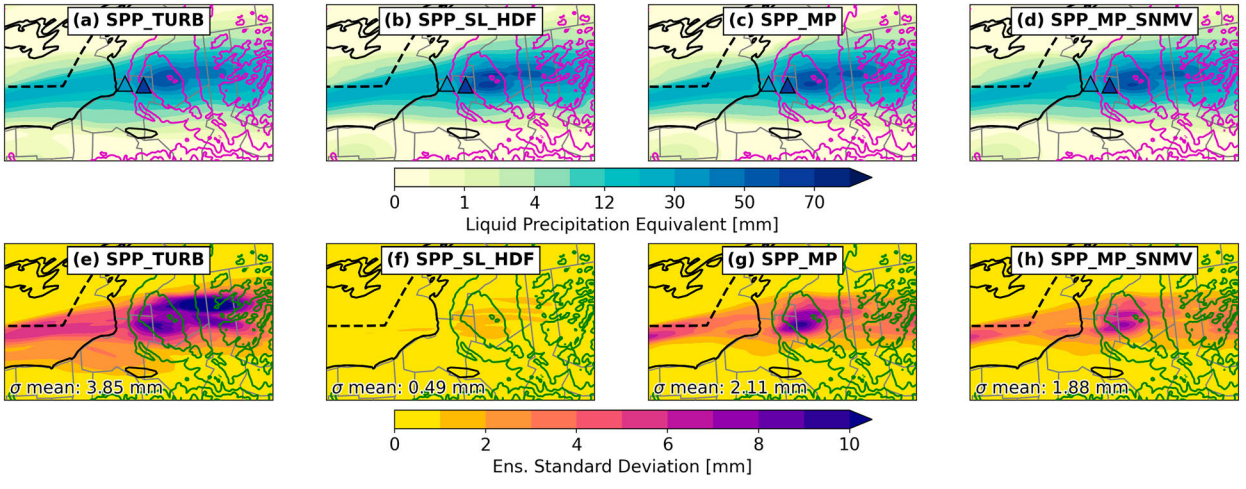

FIG. 14. SPP sensitivity experiment ensemble precipitation overview for the 24-h period ending at 0000 UTC 12 Dec 2013. (a)–(d) Ensemble mean (fill) and (e)–(h) ensemble STDEV (fill). Observed LPE amounts from two manual observing sites are plotted on all ensemble mean panels following the same color scale. STDEV values are plotted for each ensemble, averaging over the box shown in Fig. 1b. Magenta contours in (a)–(d) and green contours in (e)–(h) denote the model terrain height every 200 m.

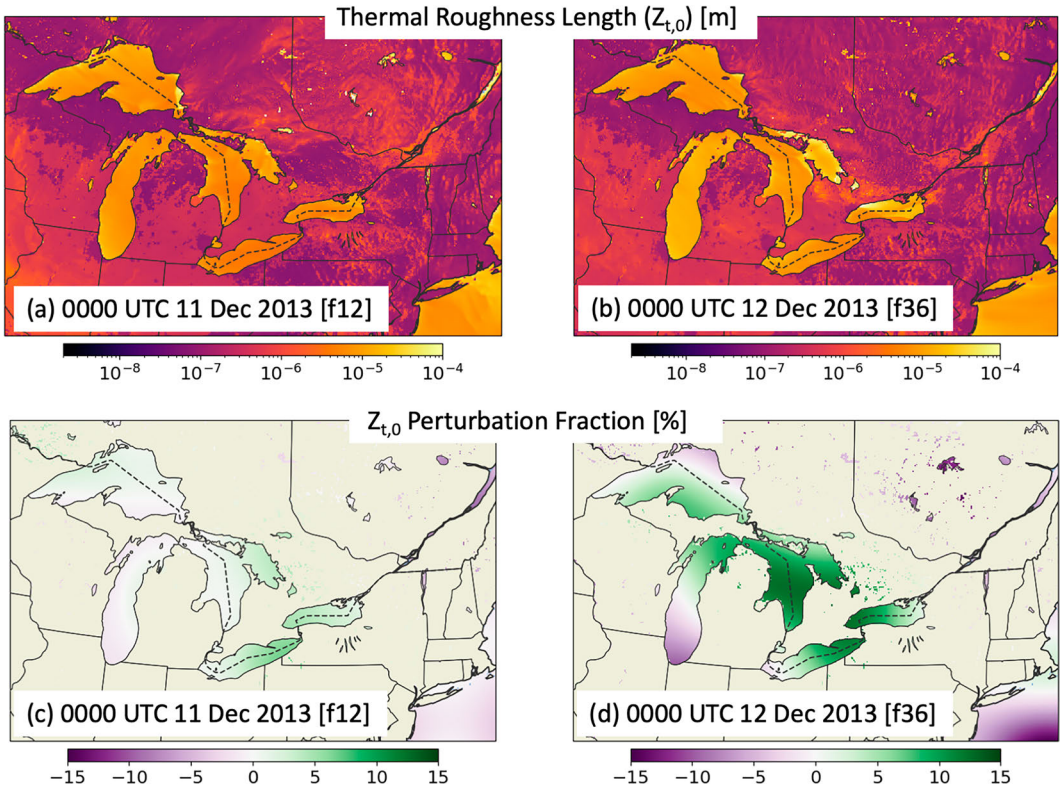

FIG. 15. (a),(b) Comparison of thermal roughness lengths from SPP_SL_HDF ensemble member 1 at two different forecast hours. (c),(d) Perturbation fraction of thermal roughness lengths, calculated as the percentage difference between the perturbed and original thermal roughness length at a given forecast hour. Note that thermal roughness lengths are perturbed over both land and water in the model, but perturbation fractions are only shown in this figure over water for clarity.

The c_p is the specific heat of air at constant pressure; u_* is the roughness Reynolds number; κ is the von Kármán constant; and P_R is the turbulent Prandtl number under neutral stability conditions, assumed to be equal to 0.4 and 1, respectively. The ψ_h is the dimensionless similarity stability function.

Figures 15a and 15b show $z_{0,t}$ over the Great Lakes at two representative forecast times from SPP_SL_HDF ensemble member 1. The $z_{0,t}$ values are lowest over land and highest over water where sensible heat fluxes are higher. Figures 15c and 15d show the percentage perturbations to $z_{0,t}$ values over water. Perturbations vary with time and space, growing larger at increasing lead times. They range from ±10% to 15%.

To estimate the magnitude of perturbations to F_H over Lake Ontario based on these 10%–15% perturbations to $z_{0,t}$, lake-average values from the SPP_SL_HDF ensemble member 1 simulations are approximated and used in Eq. (3). The ψ_h is assumed to be zero, due to the convective overlake environment. Since C_h is proportional to F_H, a 10%–15% perturbation to $z_{0,t}$ is estimated to produce F_H variations up to ±1%. Perturbation analysis of $z_{0,q}$ also yields small estimated variations in sensible moisture fluxes. This small range helps to explain the limited ensemble spread in surface fluxes, boundary layer conditions, and precipitation from SPP_SL_HDF.

While limited ensemble spread in SPP_SL_HDF is an unexpected result, it may help to explain the interaction of SPP–SL and SPP–PBL perturbations in our ensemble forecasts. Specifically, increased variation in PBL mixing due to SPP_TURB likely causes indirect variations in surface fluxes through modification of near-surface wind, temperature, or stability. These results also suggest an avenue for future work in better tuning SPP_TURB perturbations over water during LeS. In particular, SPP–SL perturbation magnitudes would likely need to be substantially increased to better represent flux uncertainty in LeS events, as multiphysics ensembles have simulated fluxes varying by as much as a factor of 2 (Conrick et al. 2015; Minder et al. 2020).

2) Role of snow mass–diameter and fall speed–diameter perturbations

We hypothesize that precipitation spread for lake-effect snow will be most sensitive to MP perturbations that affect snow properties, specifically the mass–diameter and fall speed–diameter perturbations introduced in the appendix. These perturbations specifically target uncertainties in snow properties that relate to crystal habit and degree of riming. Previous sensitivity experiments targeting snow parameters show that parameterized snow properties, especially terminal fall speed,

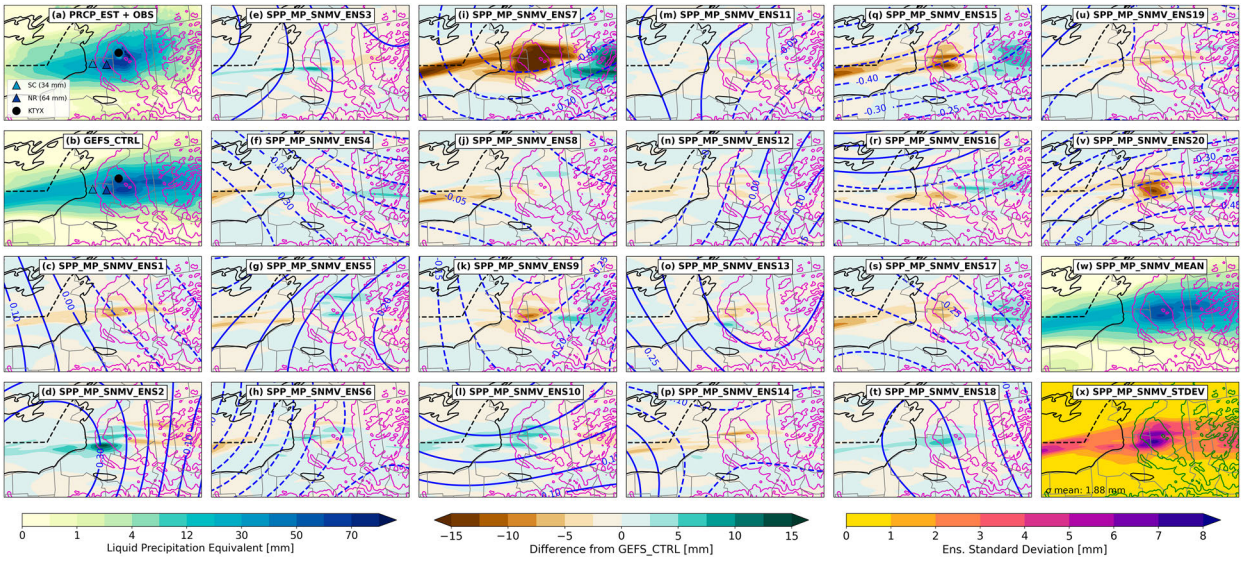

FIG. 16. As in Fig. 10, but for the SPP_MP_SNMV ensemble. Blue contours denote 24-h average SPP–MP pattern values at the lowest model level for each ensemble member.

can strongly impact the spatial structure of mesoscale precipitation features for orographic precipitation (Colle et al. 2005; Woods et al. 2007; Morales et al. 2018) and lake-effect snow (Bartolini 2019, 2023). We expect these perturbations to dominate because ice-phase precipitation processes were most active during this case, with simulated precipitation type dominated by snow (Campbell and Steenburgh 2017; Bartolini 2019). We further hypothesize that these perturbations will lead to along-wind (east–west) shifts in the forecast precipitation maximum, due to their impact on snow sedimentation rates, which affect the inland advection of falling snow (with slower fall speeds leading to greater inland extent of snowfall). To test these hypotheses, we examine the results from the SPP_MP_SNMV ensemble, a modified version of SPP_MP where only perturbations to snow mass–diameter and terminal fall velocity–diameter relations are active, comparing results with those from the full SPP_MP ensemble.

Figure 16 shows total precipitation differences relative to CTRL overlaid with mean SPP–MP pattern values for each SPP_MP_SNMV ensemble member. Differences in total precipitation between members are relatively small, about 75% smaller than the member-to-member differences found in GEFS_ICBC and ALLSPP (Figs. 10 and 11). The main precipitation signature is a west–east-oriented dipole pattern, with some members having decreased precipitation over Tug Hill (e.g., members 7, 15, 20) and others having increased precipitation over Tug Hill (e.g., members 2, 10, 18). Members with decreased windward precipitation have negative SPP field values in the vicinity of Tug Hill, while members with increased precipitation have positive SPP values. Negative perturbations to snow mass–diameter and velocity–diameter coefficients reduce the magnitude of the scale factor in each equation ($a_{m,s}$ and $a_{v,s}$, respectively), so mass and fall velocity are decreased for a given particle diameter. In particular, decreased snowfall speed leads to decreased sedimentation rates, increased precipitation residence time, and increased horizontal advection of snow, so precipitation is reduced windward of and over Tug Hill and increased leeward of Tug Hill.

To quantify the relationship between stochastic perturbation values and windward precipitation, Fig. 17 depicts the scatterplots of the 24-h mean SPP field versus the 24-h total precipitation for each SPP_MP and SPP_MP_SNMV ensemble member, averaged over the windward region of Tug Hill. A large correlation ($r^2 > 0.85$) is found between the SPP field values and precipitation for SPP_MP, due to the combined effects of all perturbed parameters. However, most of the spread in SPP values and precipitation remains for SPP_MP_SNMV with a similar correlation, due solely to the snow *M–D* and *V–D* perturbations. This supports our hypothesis regarding the primary influence of perturbed snow properties on the forecasts.

4. Discussion and conclusions

In this study, ensemble experiments were performed for a lake-effect snow (LeS) case study downwind of Lake Ontario from 11 December 2013, which was observed as part of the Ontario Winter Lake-effect Systems (OWLeS) field campaign. The Weather Research and Forecasting (WRF) Model configuration used was based loosely on the experimental High-Resolution Rapid Refresh Ensemble (HRRRE). A suite of 20-member ensembles were run using a variety of stochastic parameter perturbations (SPPs) and initial and boundary condition (IC/BC) perturbations. The SPPs included novel perturbations to the representation of snow properties in the microphysics scheme. Ensemble configurations tested include those with only SPP, with only IC/BC perturbations, and with combinations of both stochastic and IC/BC perturbations. Forecasts with lead times of 24–48 h are analyzed, emulating the current lead time of the operational HRRR and experimental HRRRE.

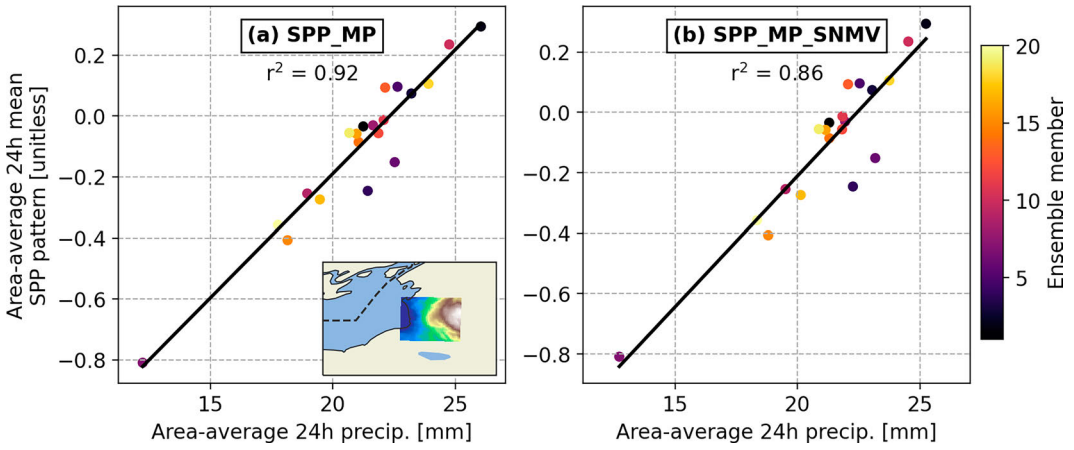

FIG. 17. Scatterplot of ensemble member 24-h average SPP pattern values and 24-h total precipitation over the windward portion of Tug Hill, for (a) SPP_MP and (b) SPP_MP_SNMV ensembles during IOP2b. Points represent an area-average value for each ensemble member, with the selected windward region shown in the inset map.

Precipitation amounts and locations are generally well forecast, with only modest ensemble mean biases near the precipitation maximum for all ensemble configurations. Differences in ensemble spread among the SPP and IC/BC configurations vary by about a factor of 2. All ensembles were found to be underdispersive, with spread/skill ratios less than 1. The ensemble that combined a suite of SPPs with IC/BC perturbations produced the most spread and the highest spread/skill ratios, consistent with other ensemble configuration studies that suggest that both stochastic physics and IC/BC perturbations are necessary to improve ensemble performance (e.g., Romine et al. 2014; Jankov et al. 2017, 2019; Kalina et al. 2021). The ensemble using a full suite of SPPs but no IC/BC perturbations (ALLSPP) showed greater spread and less error than the IC/BC-only ensemble (GEFS_ICBC). Results from an ensemble applying SPP only to turbulence and diffusion parameterizations (SPP_TURB) indicate that those perturbations provided the dominant source of spread in the full ALLSPP experiment, emphasizing the importance of these processes for LeS.

Beyond evaluation, our investigation of ensemble spread differences in each case study also revealed insights into the multiscale processes that affect snowfall predictability. Analysis of LeS band position and lake-average wind direction in each event revealed a correlation between the two, with the largest correlation for ensembles with IC/BC perturbations that have larger and faster-growing spread in both band position and wind direction, due in part to more substantial spread in the synoptic-scale flow pattern. Synoptic-scale differences in spread across the Great Lakes between an ensemble using all SPP schemes and no IC/BC perturbations (ALLSPP) and an ensemble using only IC/BC perturbations (GEFS_ICBC) show that SPP had a very little contribution to synoptic-scale spread at mid- and upper-tropospheric levels. However, the contributions of ALLSPP and GEFS_ICBC spread were nearly equal for surface fluxes across the Great Lakes.

Through sensitivity experiments targeting components of the SPP, we found that several parameters are particularly important for driving spread in LeS events. In experiments disabling SPP from the PBL scheme (leaving only SPP active in the surface layer and horizontal diffusion schemes), spreads in surface fluxes and precipitation were greatly diminished. The analysis of these results suggests that SPP in the MYNN SL scheme could benefit from additional tuning of surface roughness perturbations over water to accurately represent known uncertainty in parameterized surface fluxes during LeS events (e.g., Fujisaki-Manome et al. 2017; Minder et al. 2020). In sensitivity experiments targeting SPP within the MP scheme, we find that perturbations to snow mass–diameter and fall velocity–diameter coefficients added as part of this study substantially increase the precipitation spread relative to the baseline SPP–MP configuration from Thompson et al. (2021). Precipitation differences resemble a dipole pattern, with increased or decreased windward precipitation, associated with perturbations to snowfall velocities that affect downwind advection. These parameter perturbation additions roughly simulate variations in snow crystal habit or partial riming of snowflakes, which are known uncertainties in LeS storms (e.g., Reeves and Dawson 2013; Bartolini 2019; Jensen et al. 2020).

A similar analysis of a second OWLeS case study by Bartolini (2023) showed results largely consistent with those presented here. Taken together, these results suggest that SPP, especially when applied to turbulence and microphysical parameterizations, has the potential to improve high-resolution ensemble forecasts of LeS by strategically targeting uncertain parameterized processes in a physically consistent manner. Our results also suggest that implementing novel perturbations to snow properties (as done here) and tuning perturbations to surface roughness over water is a promising pathway to further improve SPP performance for such storms. Further work is needed to see how SPP performs for LeS over a larger sample of storms, for other winter weather types, and within operational modeling systems.

Acknowledgments. The research presented here was supported by NOAA Grant NA19OAR4590137. Jim Steenburgh,

TABLE A1. Summary of new SPPs added to the TE14 scheme as part of this study.

Parameter name	Abbreviation	Perturbation range	Notes
Snow mass–diameter coefficients	a_{m_s}, b_{m_s}	1×10^{-3}–3×10, 1.35–2.6	Coupled with snow *V–D* perturbations
Snow velocity–diameter coefficients	a_{v_s}, b_{v_s}	0.01–95, 0.01–0.6	Coupled with snow *M–D* perturbations
Snow capacitance	C_s	0.2–0.5	

Ryan Torn, Kara Sulia, and Robert Fovell provided valuable scientific feedback on an earlier version of the manuscript. Joe Olson and Isidora Jankov provided consultations regarding the setup of the HRRRE-like WRF configuration used. Robert Conrick and Greg Thompson provided helpful information and suggestions regarding SPP implementation. The manuscript benefited from the comments of three anonymous reviewers.

Data availability statement. The observational datasets used are available via the data archives cited in the manuscript and provided in the reference list. The foundational WRF-ARW code used is available at https://doi.org/10.5065/D6MK6B4K. A version of the WRF code with the SPP additions presented here is available at https://github.com/mbartolini18/WRFV4_spp.

APPENDIX

Formulation of Novel Snow SPP Perturbations

Previous studies have shown that cool season mesoscale precipitation forecasts can exhibit large sensitivities to the representation of snow properties in MP parameterizations (e.g., Woods et al. 2007; Morales et al. 2018; Bartolini 2019; Gaudet et al. 2021). Such sensitivities were documented specifically for OWLeS IOP2b by Bartolini (2023), using fixed-parameter perturbation experiments. Motivated by the results of these studies, we implement new stochastic perturbations to snow capacitance, mass–diameter (*M–D*), and fall velocity–diameter (*V–D*) coefficients within TE14. These perturbations are meant, in part, to represent the inherent uncertainty associated with the formulation of most bulk microphysics schemes, which do not explicitly account for variations in snow crystal habit and/or partial riming.

Table A1 summarizes our SPP additions to the original TE14 SPP–MP configuration described by Thompson et al. (2021). Snow capacitance C_s perturbations are implemented as an additive perturbation, bounded by capacitance values for plate-like and spherical particles, following the snow deposition and sublimation parameterization of Srivastava and Coen (1992).

Perturbations to *M–D* and *V–D* relationships require a more-complex SPP formulation in TE14. Within TE14, these relationships are represented by

$$M = a_{m,s} D^{b_{m,s}}, \tag{A1}$$

$$V = a_{v,s} D^{b_{v,s}} e^{-f_{v,s}}, \tag{A2}$$

where M and V are the mass and terminal fall speed, respectively, for a snow particle of equivalent spherical diameter D. In TE14, $a_{m,s}$, $b_{m,s}$, $a_{v,s}$, $b_{v,s}$, and $f_{v,s}$ are constants. However, the appropriate value for these coefficients depends on crystal habit and snow density. Figure A1 shows several snow *M–D* and *V–D* coefficient pairs for different observed crystal habits, which include the default parameters from TE14 and parameter sets representing various snow habits used in Woods et al. (2007).

To represent the uncertainty in these relationships, we perturb the values $a_{m,s}$ and $a_{v,s}$ directly and then prescribe

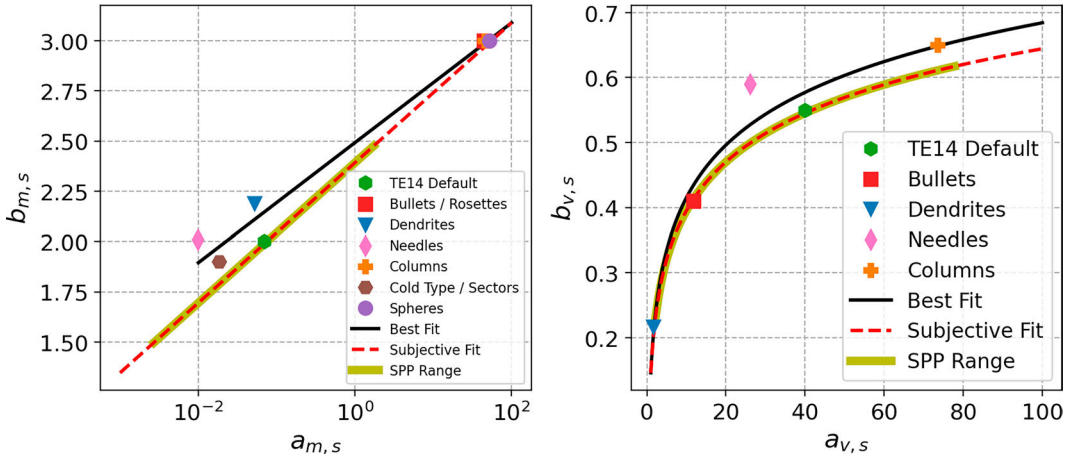

FIG. A1. Scatterplots of mass–diameter and velocity–diameter coefficients. Points indicate empirical relations for different crystal habits from Woods et al. (2007) and default values in TE14 (blue markers). Black lines indicate linear regression lines fit for all points. Red dashed lines denote manually adjusted linear regression curves to pass through default TE14 values, with yellow segments on each line representing an SPP range of ±2 STDEVs.

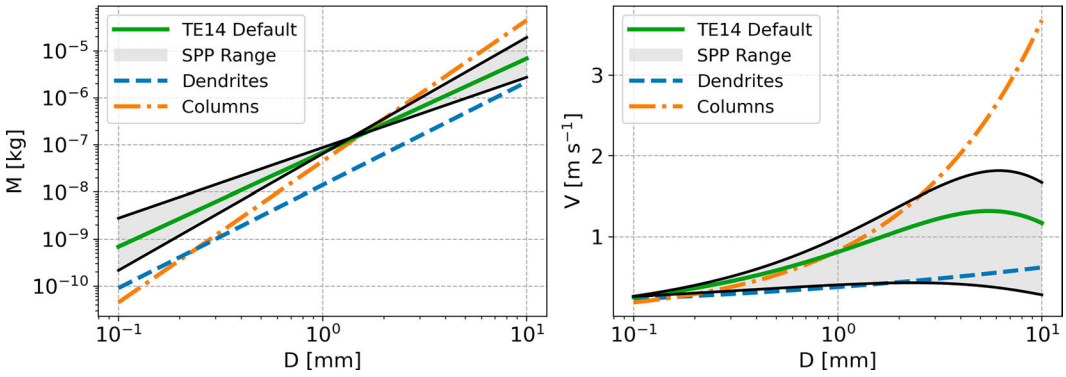

FIG. A2. Comparison of snow mass–diameter and velocity–diameter relations, compared to the default curves used in TE14 (green solid lines). Blue dashed and orange dot–dashed lines represent mass–diameter and velocity–diameter relations for dendrites and columns, respectively. The gray shaded area bounded by black lines represents a perturbed SPP range of ±2 STDEVs.

values of $b_{m,s}$ and $b_{v,s}$ based on linear regression curves fitted through the parameter sets in Fig. A1. This approach is used to maintain consistency between the *M–D* and *V–D* relations. However, linear regression coefficients are adjusted (dashed red lines) so that an SPP perturbation of zero returns the original TE14 *M–D* and *V–D*. This choice is made so that leaving SPP inactive does not change the scheme's default behavior, consistent with the design of the other MP SPP from Thompson et al. (2021). The range of coefficient values used in the experiments is shown in Fig. A1, and the effect of these perturbed values on *M–D* and *V–D* relations is shown in Fig. A2 (with relationships for other fixed parameter pairs shown for comparison). For simplicity, we fix $f_{v,s}$ at its default value (100), although this parameter is also likely uncertain. Since snow *M–D* and *V–D* perturbations affect various MP process calculations, additional modifications were implemented to ensure consistent treatment throughout the code, including to the lookup table used for collection calculations. More details on the implementation of SPP for *M–D* and *V–D* are given in Bartolini (2023).

REFERENCES

Alcott, T. I., W. J. Steenburgh, and N. F. Laird, 2012: Great Salt Lake–effect precipitation: Observed frequency, characteristics, and associated environmental factors. *Wea. Forecasting*, **27**, 954–971, https://doi.org/10.1175/WAF-D-12-00016.1.

Bartolini, W. M., 2019: Convection-permitting ensemble forecasts of the 10–12 December 2013 lake-effect snow event: Sensitivity to microphysical, planetary boundary layer, and surface layer parameterizations. M.S. thesis, Dept. of Atmospheric and Environmental Sciences, State University of New York, 99 pp., https://scholarsarchive.library.albany.edu/legacy-etd/2220/.

——, 2023: Using stochastic physics perturbations in ensemble forecasts to investigate predictability of mesoscale winter precipitation events. Ph.D. thesis, State University of New York, 199 pp., https://www.proquest.com/dissertations-theses/using-stochastic-physics-perturbations-ensemble/docview/2814301423/se-2.

Benjamin, S. G., and Coauthors, 2016: A North American hourly assimilation and model forecast cycle: The Rapid Refresh. *Mon. Wea. Rev.*, **144**, 1669–1694, https://doi.org/10.1175/MWR-D-15-0242.1.

Bergmaier, P. T., and B. Geerts, 2020: LLAP Band structure and intense lake-effect snowfall downwind of Lake Ontario: Insights from the OWLeS 7–9 January 2014 Event. *J. Appl. Meteor. Climatol.*, **59**, 1691–1715, https://doi.org/10.1175/JAMC-D-19-0288.1.

——, ——, L. S. Campbell, and W. J. Steenburgh, 2017: The OWLeS IOP2b lake-effect snowstorm: Dynamics of the secondary circulation. *Mon. Wea. Rev.*, **145**, 2437–2459, https://doi.org/10.1175/MWR-D-16-0462.1.

Berner, J., K. R. Fossell, S.-Y. Ha, J. P. Hacker, and C. Snyder, 2015: Increasing the skill of probabilistic forecasts: Understanding performance improvements from model-error representations. *Mon. Wea. Rev.*, **143**, 1295–1320, https://doi.org/10.1175/MWR-D-14-00091.1.

Brown, R. A., T. A. Niziol, N. R. Donaldson, P. I. Joe, and V. T. Wood, 2007: Improved detection using negative elevation angles for mountaintop WSR-88Ds. Part III: Simulations of shallow convective activity over and around Lake Ontario. *Wea. Forecasting*, **22**, 839–852, https://doi.org/10.1175/WAF1019.1.

Buizza, R., 1997: Potential forecast skill of ensemble prediction and spread and skill distributions of the ECMWF Ensemble Prediction System. *Mon. Wea. Rev.*, **125**, 99–119, https://doi.org/10.1175/1520-0493(1997)125<0099:PFSOEP>2.0.CO;2.

Campbell, L. S., and W. J. Steenburgh, 2017: The OWLeS IOP2b lake-effect snowstorm: Mechanisms contributing to the Tug Hill precipitation maximum. *Mon. Wea. Rev.*, **145**, 2461–2478, https://doi.org/10.1175/MWR-D-16-0461.1.

——, ——, P. G. Veals, T. W. Letcher, and J. R. Minder, 2016: Lake-effect mode and precipitation enhancement over the Tug Hill Plateau during OWLeS IOP2b. *Mon. Wea. Rev.*, **144**, 1729–1748, https://doi.org/10.1175/MWR-D-15-0412.1.

Chu, P. Y., J. G. W. Kelley, G. V. Mott, A. Zhang, and G. A. Lang, 2011: Development, implementation, and skill assessment of the NOAA/NOS Great Lakes Operational Forecast System. *Ocean Dyn.*, **61**, 1305–1316, https://doi.org/10.1007/s10236-011-0424-5.

Colle, B. A., M. F. Garvert, J. B. Wolfe, C. F. Mass, and C. P. Woods, 2005: The 13–14 December 2001 IMPROVE-2 event.

Part III: Simulated microphysical budgets and sensitivity studies. *J. Atmos. Sci.*, **62**, 3535–3558, https://doi.org/10.1175/JAS3552.1.

Conrick, R., H. D. Reeves, and S. Zhong, 2015: The dependence of QPF on the choice of boundary- and surface-layer parameterization for a lake-effect snowstorm. *J. Appl. Meteor. Climatol.*, **54**, 1177–1190, https://doi.org/10.1175/JAMC-D-14-0291.1.

Dowell, D. C., and Coauthors, 2022: The High-Resolution Rapid Refresh (HRRR): An hourly updating convection-allowing forecast model. Part I: Motivation and system description. *Wea. Forecasting*, **37**, 1371–1395, https://doi.org/10.1175/WAF-D-21-0151.1.

Fujisaki-Manome, A., and Coauthors, 2017: Turbulent heat fluxes during an extreme lake-effect snow event. *J. Hydrometeor.*, **18**, 3145–3163, https://doi.org/10.1175/JHM-D-17-0062.1.

Gaudet, L. C., K. J. Sulia, T.-C. Tsai, J.-P. Chen, and J. P. Blair, 2021: Assessment of a microphysical ensemble used to investigate the OWLeS IOP4 lake-effect storm. *J. Atmos. Sci.*, **78**, 1607–1628, https://doi.org/10.1175/JAS-D-20-0045.1.

Gerbush, M. R., D. A. R. Kristovich, and N. F. Laird, 2008: Mesoscale boundary layer and heat flux variations over pack ice–covered Lake Erie. *J. Appl. Meteor. Climatol.*, **47**, 668–682, https://doi.org/10.1175/2007JAMC1479.1.

Gowan, T. M., W. J. Steenburgh, and J. R. Minder, 2021: Downstream evolution and coastal-to-inland transition of landfalling lake-effect systems. *Mon. Wea. Rev.*, **149**, 1023–1040, https://doi.org/10.1175/MWR-D-20-0253.1.

——, ——, and ——, 2022: Orographic effects on landfalling lake-effect systems. *Mon. Wea. Rev.*, **150**, 2013–2031, https://doi.org/10.1175/MWR-D-21-0314.1.

Grell, G. A., and S. R. Freitas, 2014: A scale and aerosol aware stochastic convective parameterization for weather and air quality modeling. *Atmos. Chem. Phys.*, **14**, 5233–5250, https://doi.org/10.5194/acp-14-5233-2014.

Jankov, I., and Coauthors, 2017: A performance comparison between multiphysics and stochastic approaches within a North American RAP ensemble. *Mon. Wea. Rev.*, **145**, 1161–1179, https://doi.org/10.1175/MWR-D-16-0160.1.

——, J. Beck, J. Wolff, M. Harrold, J. B. Olson, T. Smirnova, C. Alexander, and J. Berner, 2019: Stochastically perturbed parameterizations in an HRRR-based ensemble. *Mon. Wea. Rev.*, **147**, 153–173, https://doi.org/10.1175/MWR-D-18-0092.1.

Jensen, A. A., P. T. Bergmaier, B. Geerts, H. Morrison, and L. S. Campbell, 2020: Sensitivity of convective cell dynamics and microphysics to model resolution for the OWLeS IOP2b lake-effect snowband. *Mon. Wea. Rev.*, **148**, 3305–3328, https://doi.org/10.1175/MWR-D-19-0320.1.

Kalina, E. A., I. Jankov, T. Alcott, J. Olson, J. Beck, J. Berner, D. Dowell, and C. Alexander, 2021: A progress report on the development of the High-Resolution Rapid Refresh Ensemble. *Wea. Forecasting*, **36**, 791–804, https://doi.org/10.1175/WAF-D-20-0098.1.

Kristovich, D. A. R., and Coauthors, 2017: The Ontario Winter Lake-effect Systems field campaign: Scientific and educational adventures to further our knowledge and prediction of lake-effect storms. *Bull. Amer. Meteor. Soc.*, **98**, 315–332, https://doi.org/10.1175/BAMS-D-15-00034.1.

——, L. Bard, L. Stoecker, and B. Geerts, 2018: Influence of Lake Erie on a Lake Ontario lake-effect snowstorm. *J. Appl. Meteor. Climatol.*, **57**, 2019–2033, https://doi.org/10.1175/JAMC-D-17-0349.1.

Laird, N., R. Sobash, and N. Hodas, 2009: The frequency and characteristics of lake-effect precipitation events associated with the New York State Finger lakes. *J. Appl. Meteor. Climatol.*, **48**, 873–886, https://doi.org/10.1175/2008JAMC2054.1.

Laird, N. F., N. D. Metz, L. Gaudet, C. Grasmick, L. Higgins, C. Loeser, and D. A. Zelinsky, 2017: Climatology of cold season lake-effect cloud bands for the North American Great Lakes. *Int. J. Climatol.*, **37**, 2111–2121, https://doi.org/10.1002/joc.4838.

Lang, C. E., J. M. McDonald, L. Gaudet, D. Doeblin, E. A. Jones, and N. F. Laird, 2018: The influence of a lake-to-lake connection from Lake Huron on the lake-effect snowfall in the vicinity of Lake Ontario. *J. Appl. Meteor. Climatol.*, **57**, 1423–1439, https://doi.org/10.1175/JAMC-D-17-0225.1.

Menne, M. J., I. Durre, R. S. Vose, B. E. Gleason, and T. G. Houston, 2012a: An overview of the Global Historical Climatology Network-Daily database. *J. Atmos. Oceanic Technol.*, **29**, 897–910, https://doi.org/10.1175/JTECH-D-11-00103.1.

——, and Coauthors, 2012b: Global Historical Climatology Network—Daily (GHCN-Daily), version 3. NOAA National Climatic Data Center, accessed 23 February 2023, https://doi.org/10.7289/V5D21VHZ.

Minder, J. R., T. W. Letcher, L. S. Campbell, P. G. Veals, and W. J. Steenburgh, 2015: The evolution of lake-effect convection during landfall and orographic uplift as observed by profiling radars. *Mon. Wea. Rev.*, **143**, 4422–4442, https://doi.org/10.1175/MWR-D-15-0117.1.

——, W. M. Bartolini, C. Spence, N. R. Hedstrom, P. D. Blanken, and J. D. Lenters, 2020: Characterizing and constraining uncertainty associated with surface and boundary layer turbulent fluxes in simulations of lake-effect snowfall. *Wea. Forecasting*, **35**, 467–488, https://doi.org/10.1175/WAF-D-19-0153.1.

Morales, A., H. Morrison, and D. J. Posselt, 2018: Orographic precipitation response to microphysical parameter perturbations for idealized moist nearly neutral flow. *J. Atmos. Sci.*, **75**, 1933–1953, https://doi.org/10.1175/JAS-D-17-0389.1.

Nakai, S., K. Iwanami, R. Misumi, S.-G. Park, and T. Kobayashi, 2005: A classification of snow clouds by Doppler radar observations at Nagaoka, Japan. *SOLA*, **1**, 161–164, https://doi.org/10.2151/sola.2005-042.

Nakanishi, M., and H. Niino, 2006: An improved Mellor–Yamada level-3 model: Its numerical stability and application to a regional prediction of advection fog. *Bound.-Layer Meteor.*, **119**, 397–407, https://doi.org/10.1007/s10546-005-9030-8.

Niziol, T. A., W. R. Snyder, and J. S. Waldstreicher, 1995: Winter weather forecasting throughout the eastern United States. Part IV: Lake effect snow. *Wea. Forecasting*, **10**, 61–77, https://doi.org/10.1175/1520-0434(1995)010%3C0061:WWFTTE%3E2.0.CO;2.

NOAA Great Lakes Environmental Research Laboratory, 2014: NOAA Great Lakes Coastal Forecasting System (GLCFS), Nowcast Data NOAA/GLERL, https://www.glerl.noaa.gov/emf/GLCFS_POM_archive/.

NOAA-National Center for Environmental Prediction, 2017: Global Ensemble Forecast System (GEFS) analysis. NOAA National Centers for Environmental Information, accessed 10 February 2021, https://www.ncei.noaa.gov/products/weather-climate-models/global-ensemble-forecast.

Norris, J., G. Vaughan, and D. M. Schultz, 2013: Snowbands over the English Channel and Irish Sea during cold-air outbreaks. *Quart. J. Roy. Meteor. Soc.*, **139**, 1747–1761, https://doi.org/10.1002/qj.2079.

NWS, 1991: NOAA Next Generation Radar (NEXRAD) level 2 base data. NOAA National Centers for Environmental Information, https://doi.org/10.7289/V5W9574V.

Reeves, H. D., and D. T. Dawson III, 2013: The dependence of QPF on the choice of microphysical parameterization for lake-effect snowstorms. *J. Appl. Meteor. Climatol.*, **52**, 363–377, https://doi.org/10.1175/JAMC-D-12-019.1.

Roberts, B., B. T. Gallo, I. L. Jirak, A. J. Clark, D. C. Dowell, X. Wang, and Y. Wang, 2020: What does a convection-allowing ensemble of opportunity buy us in forecasting thunderstorms? *Wea. Forecasting*, **35**, 2293–2316, https://doi.org/10.1175/WAF-D-20-0069.1.

Romine, G. S., C. S. Schwartz, J. Berner, K. R. Fossell, C. Snyder, J. L. Anderson, and M. L. Weisman, 2014: Representing forecast error in a convection-permitting ensemble system. *Mon. Wea. Rev.*, **142**, 4519–4541, https://doi.org/10.1175/MWR-D-14-00100.1.

Saslo, S., and S. J. Greybush, 2017: Prediction of lake-effect snow using convection-allowing ensemble forecasts and regional data assimilation. *Wea. Forecasting*, **32**, 1727–1744, https://doi.org/10.1175/WAF-D-16-0206.1.

Skamarock, W. C., and Coauthors, 2008: A description of the Advanced Research WRF version 3. NCAR Tech. Note NCAR/TN-475+STR, 113 pp., https://doi.org/10.5065/D68S4MVH.

Smith, A. B., 2023: U.S. billion–dollar weather and climate disasters, 1980–present (NCEI accession 0209268). https://doi.org/10.25921/stkw-7w73.

Srivastava, R. C., and J. L. Coen, 1992: New explicit equations for the accurate calculation of the growth and evaporation of hydrometeors by the diffusion of water vapor. *J. Atmos. Sci.*, **49**, 1643–1651, https://doi.org/10.1175/1520-0469(1992)049<1643:NEEFTA>2.0.CO;2.

Steenburgh, J., L. Campbell, and P. Veals, 2014a: North Redfield snow study station data, version 1.0. UCAR/NCAR—Earth Observing Laboratory, https://doi.org/10.5065/d68051cn.

——, ——, and ——, 2014b: Sandy Creek snow study station data, version 1.0. UCAR/NCAR—Earth Observing Laboratory, https://doi.org/10.5065/D68K77WG.

——, ——, and ——, 2014c: OWLeS: University of Utah North Redfield radiosonde data, version 1.0. UCAR/NCAR—Earth Observing Laboratory, https://doi.org/10.26023/RH2Y-8E1R-G905.

Steenburgh, W. J., and L. S. Campbell, 2017: The OWLeS IOP2b lake-effect snowstorm: Shoreline geometry and the mesoscale forcing of precipitation. *Mon. Wea. Rev.*, **145**, 2421–2436, https://doi.org/10.1175/MWR-D-16-0460.1.

——, and S. Nakai, 2020: Perspectives on sea- and lake-effect precipitation from Japan's "Gosetsu Chitai". *Bull. Amer. Meteor. Soc.*, **101**, E58–E72, https://doi.org/10.1175/BAMS-D-18-0335.1.

Thompson, G., and T. Eidhammer, 2014: A study of aerosol impacts on clouds and precipitation development in a large winter cyclone. *J. Atmos. Sci.*, **71**, 3636–3658, https://doi.org/10.1175/JAS-D-13-0305.1.

——, J. Berner, M. Frediani, J. A. Otkin, and S. M. Griffin, 2021: A stochastic parameter perturbation method to represent uncertainty in a microphysics scheme. *Mon. Wea. Rev.*, **149**, 1481–1497, https://doi.org/10.1175/MWR-D-20-0077.1.

Vasiloff, S., 2001: WSR-88D performance in northern Utah during the winter of 1998–1999. NOAA/Western Regional Tech. Attachment 01–02, 8 pp., https://www.weather.gov/media/wrh/online_publications/TAs/ta0103.pdf.

Veals, P. G., W. J. Steenburgh, and L. S. Campbell, 2018: Factors Affecting the inland and orographic enhancement of lake-effect precipitation over the Tug Hill Plateau. *Mon. Wea. Rev.*, **146**, 1745–1762, https://doi.org/10.1175/MWR-D-17-0385.1.

Welsh, D., B. Geerts, X. Jing, P. T. Bergmaier, J. R. Minder, W. J. Steenburgh, and L. S. Campbell, 2016: Understanding heavy lake-effect snowfall: The vertical structure of radar reflectivity in a deep snowband over and downwind of Lake Ontario. *Mon. Wea. Rev.*, **144**, 4221–4244, https://doi.org/10.1175/MWR-D-16-0057.1.

Woods, C. P., M. T. Stoelinga, and J. D. Locatelli, 2007: The IMPROVE-1 storm of 1–2 February 2001. Part III: Sensitivity of a mesoscale model simulation to the representation of snow particle types and testing of a bulk microphysical scheme with snow habit prediction. *J. Atmos. Sci.*, **64**, 3927–3948, https://doi.org/10.1175/2007JAS2239.1.

Wright, D. M., D. J. Posselt, and A. L. Steiner, 2013: Sensitivity of lake-effect snowfall to lake ice cover and temperature in the Great Lakes region. *Mon. Wea. Rev.*, **141**, 670–689, https://doi.org/10.1175/MWR-D-12-00038.1.

Xue, P., J. S. Pal, X. Ye, J. D. Lenters, C. Huang, and P. Y. Chu, 2017: Improving the simulation of large lakes in regional climate modeling: Two-way lake–atmosphere coupling with a 3D hydrodynamic model of the Great Lakes. *J. Climate*, **30**, 1605–1627, https://doi.org/10.1175/JCLI-D-16-0225.1.

Zhao, L., J. Jin, S.-Y. Wang, and M. B. Ek, 2012: Integration of remote-sensing data with WRF to improve lake-effect precipitation simulations over the Great Lakes region. *J. Geophys. Res.*, **117**, D09102, https://doi.org/10.1029/2011JD016979.